1 *Research article*

2

3

4 **Progressive axonopathy when oligodendrocytes lack the myelin protein CMTM5**

5

6

7 Tobias J. Buscham[1], Maria A. Eichel-Vogel[1], Anna M. Steyer[1,2], Olaf Jahn[3,4],

8 Nicola Strenzke[5], Rakshit Dardawal[6], Tor R. Memhave[6], Sophie B. Siems[1], Christina Müller[7],

9 Martin Meschkat[1,8], Ting Sun[1], Torben Ruhwedel [1,2], Wiebke Möbius[1,2],

10 Eva-Maria Krämer-Albers[7], Susann Boretius[6], Klaus-Armin Nave[1] and Hauke B. Werner[1,*]

11

12

13 **Affiliations**

14 [1]Department of Neurogenetics, Max Planck Institute of Experimental Medicine, 37075 Göttingen, Germany

15 [2]Electron Microscopy Core Unit, Max Planck Institute of Experimental Medicine, 37075 Göttingen, Germany

16 [3]Proteomics Group, Max Planck Institute of Experimental Medicine, 37075 Göttingen, Germany

17 [4]Translational Neuroproteomics Group, Department of Psychiatry and Psychotherapy, University Medical Center

18 Göttingen, Georg-August-University, 37075 Göttingen, Germany

19 [5]Institute for Auditory Neuroscience, University Medicine Göttingen, 37075 Göttingen, Germany

20 [6]Functional Imaging Laboratory, German Primate Center, Leibniz Institute for Primate Research 37077 Göttingen,

21 Germany

22 [7]Institute of Developmental Biology and Neurobiology, Johannes Gutenberg University, 55128 Mainz, Germany

23 [8]Abberior Instruments Gmbh, 37077 Göttingen, Germany

24

25

26 ***Corresponding author**

27 Dr. Hauke Werner

28 Max Planck Institute of Experimental Medicine

29 Department of Neurogenetics

30 Hermann-Rein-Str. 3; D-37075 Göttingen, Germany

31 Tel.: +49 (551) 3899-759

32 E-Mail: Hauke@em.mpg.de

33

34

35 **Keywords**

36 Oligodendrocyte; myelin sheath; axon-glia interaction; axon degeneration; neuropathology;

37 focused ion beam-scanning electron microscopy (FIB-SEM); differential myelin proteome

38 analysis

39

40 **Reviewer login information to the proteome data repository:**

41 **Project:** Progressive axonopathy when oligodendrocytes lack the myelin protein CMTM5

42 **Project accession:** PXD029443

43 **Reviewer account:** Username: reviewer_pxd029443@ebi.ac.uk; Password: 2nTEI47v

44

45 **Word and figure count**

46 3548 words (main text); 7 main figures; 6 supplemental figures, 2 tables

47

48

49 **Abstract**

50

51 Oligodendrocytes facilitate rapid impulse propagation along the axons they myelinate and

52 support their long-term integrity. However, the functional relevance of many myelin proteins

53 has remained unknown. Here we find that expression of the tetraspan-transmembrane protein

54 CMTM5 (Chemokine-like factor-like MARVEL-transmembrane domain containing protein 5) is

55 highly enriched in oligodendrocytes and CNS myelin. Genetic disruption of the *Cmtm5*-gene

56 in oligodendrocytes of mice does not impair the development or ultrastructure of CNS myelin.

57 However, oligodendroglial *Cmtm5*-deficiency causes an early-onset progressive axonopathy,

58 which we also observe in global and in tamoxifen-induced oligodendroglial *Cmtm5*-mutants.

59 Presence of the *Wld^s* mutation ameliorates the axonopathy, implying a Wallerian degeneration-

60 like pathomechanism. These results indicate that CMTM5 is involved in the function of

61 oligodendrocytes to maintain axonal integrity rather than myelin biogenesis.

62

63

Introduction

Myelination of axons by oligodendrocytes enables rapid, saltatory conduction of signals in the vertebrate central nervous system (CNS) (Cohen et al., 2020; Hartline & Colman, 2007; Tasaki, 1939). Additionally, oligodendrocytes support the long-term preservation of axons metabolically (Fünfschilling et al., 2012; Lee et al., 2012; Philips et al., 2021; Saab et al., 2016) and via extracellular vesicles (Chamberlain et al., 2021; Frühbeis et al., 2020; Mukherjee et al., 2020). In fact, myelin pathology in CNS disorders such as leukodystrophies, multiple sclerosis and respective animal models is commonly associated with axonal degeneration (Franklin et al., 2012; Stadelmann et al., 2019; Wolf et al., 2021). Oligodendrocytes are thus required to maintain axonal integrity and ultimately CNS function. However, oligodendrocytes express thousands of transcripts (Jäkel et al., 2019; Zhang et al., 2014; Zhou et al., 2020) and myelin comprises hundreds of proteins (Ishii et al., 2009; Jahn et al., 2020), and our knowledge remains limited with respect to which molecules contribute to myelin biogenesis, axonal support, or both.

We recently found that a member of the chemokine-like factor-like MARVEL-transmembrane containing (CMTM) protein family, CMTM6, is expressed in Schwann cells, the myelinating cells of the peripheral nervous system (PNS), and that its deletion in mice affects the diameters and function of peripheral axons (Eichel et al., 2020). Based on this finding we asked if a member of the CMTM family is expressed in oligodendrocytes, which may thus fulfill a similar function in the CNS. The CMTM protein family comprises eight members in humans (Han et al., 2003) that have mostly been associated with mediating tumor immunity (Burr et al., 2017; Mezzadra et al., 2017; Shao et al., 2007; Xiao et al., 2015; Yuan et al., 2020).

In this study we focused on *Cmtm5* considering (i) its expression in oligodendrocytes according to bulk RNAseq data (Zhang et al., 2014), (ii) the finding that the *Cmtm5* gene promoter drives expression of Cre recombinase in oligodendrocytes (Gong et al., 2007), and (iii) the mass spectrometric identification of CMTM5 in CNS myelin (Jahn et al., 2020). By structure prediction, CMTM5 comprises four transmembrane domains with small intracellular N- and C-terminal domains and two small extracellular loops (Jumper et al., 2021) but, its name notwithstanding, no apparent chemokine-like sequence motif. Here we assess the functional relevance of CMTM5 in oligodendrocytes. We find that CMTM5 is not required for normal myelination or axonal diameters in the CNS. However, our data indicate that CMTM5 is involved in the function of oligodendrocytes to maintain the integrity of CNS axons.

100   **Results**

101

102   **Expression of CMTM5 is enriched in oligodendrocytes and CNS myelin**

103   We explored the hypothesis that CNS myelin comprises a homolog of the recently identified

104   (Eichel et al., 2020) PNS myelin protein CMTM6. Indeed, previous mass spectrometric

105   analysis identified CMTM5 (Chemokine-like factor-like MARVEL-transmembrane domain-

106   containing family member-5) in myelin purified from the brains of C57/Bl6 mice (Jahn et al.,

107   2020). In contrast, neither CMTM6 nor any other member of the protein family was detected in

108   CNS myelin. Correspondingly, published RNA sequencing data (Zhang et al., 2014)

109   demonstrate that mature oligodendrocytes (MOL) display substantial abundance of *Cmtm5*

110   mRNA but not of any other gene family member (**Figure 1–Supplement 1A**). Indeed, *Cmtm5*

111   mRNA is enriched in the oligodendrocyte lineage, in which its abundance increases with

112   differentiation from the progenitor (OPC) stage to the MOL stage (**Figure 1–Supplement 1B**).

113   When evaluating mRNA abundance according to published scRNA-seq data (Jäkel et al.,

114   2019; Zhou et al., 2020), MOL (as annotated by high-level expression of myelin basic protein

115   mRNA, *MBP/Mbp*) express *CMTM5/Cmtm5* mRNA in both humans and mice (**Figure 1–**

116   **Supplement 1C-F**).

117

118   To independently confirm CMTM5 as a myelin protein, we first used immunoblotting to assess

119   its abundance in myelin biochemically purified from mouse brains in comparison to equal

120   amounts of mouse brain lysate. One band was detected at the expected molecular weight of

121   18 kDa. Indeed, the abundance of CMTM5 was markedly higher in the myelin-enriched fraction

122   than in brain lysates (**Figure 1A**), similar to the myelin markers PLP, CNP and SIRT2. Confocal

123   imaging of immunolabeled spinal cord sections revealed CMTM5 in CNS myelin of c57Bl/6N

124   mice (**Figure 1B**). Importantly, no labeling was found when analyzing corresponding sections

125   of newly generated conditional mouse mutants with a deletion of the *Cmtm5* gene in in

126   myelinating cells (*Cmtm5$^{fl/fl}$*Cnp$^{Cre/WT}$*, also termed cKO; see below) (**Figure 1B**). By

127   immunoblotting of homogenized wild-type mouse brains, the abundance of CMTM5 increased

128   coinciding with myelin formation and maturation between postnatal days 15 (P15) and P24

129   (**Figure 1C**). In adult mouse brains between 6 and 24 months (m) of age, the abundance of

130   CMTM5 remained unchanged (**Figure 1C**). The abundance of CMTM5 in purified myelin also

131   remained essentially constant (**Figure 1D**). Taken together, expression of CMTM5 in the CNS

132   is largely limited to oligodendrocytes and enriched in CNS myelin.

133

134   **CMTM5 is not essential for myelin biogenesis and composition**

135   To assess the functional relevance of the expression of *Cmtm5* by oligodendrocytes, we

136   generated mouse mutants with a conditional deletion of the gene selectively in myelinating

4

137 cells (*Cmtm5$^{fl/fl}$*Cnp$^{Cre/WT}$*, also termed cKO). Conditional mutants were born at expected

138 frequencies, and cKO mice showed no obvious behavioral phenotype. We biochemically

139 purified myelin from brains of cKO mice and respective controls at P75 and further examined

140 if CMTM5-deficiency affects the protein composition of myelin. By immunoblotting, CMTM5

141 was readily detected in myelin purified from the brains of control mice but undetectable in

142 *Cmtm5* cKO myelin (**Figure 2A**). By label-free quantitative proteome analysis, *Cmtm5* cKO

143 mice displayed a largely similar myelin proteome composition as control mice (**Figure 2B,B´**).

144 As an exception, CMTM5 was undetectable in myelin purified from the brains of *Cmtm5* cKO

145 mice, and the relative abundance of CNP was approximately halved as previously shown for

146 the utilized *Cnp$^{Cre/WT}$* driver mice owing to heterozygosity of the *Cnp* gene (Erwig, et al., 2019;

147 Lappe-Siefke et al., 2003).

148

149 To examine if loss of CMTM5 affects the biogenesis and ultrastructure of myelin, we used

150 transmission electron microscopy to assess optic nerves dissected from cKO and control mice

151 at P30 and P75 (**Figure 2C-L**). By morphometry, we did not observe signs of hypomyelination

152 (**Figure 2D,I**) or myelin pathology such as myelin outfoldings, inner tongue swellings or lamella

153 splittings (**Figure 2E,J**). The thickness of myelin sheaths, as determined by the g-ratio, was

154 also virtually the same in cKO and control mice (**Figure 2F-G, K-L**). By immunohistochemistry,

155 *Cmtm5* cKO mice displayed an unaltered number of cells immunopositive for carbonic

156 anhydrase 2 (CAII), a marker for mature oligodendrocytes (**Figure 2M,N**). We then used

157 magnetic resonance imaging (MRI) to assess the brains of 8-months old *Cmtm5* cKO and

158 respective control mice. However, no apparent differences in brain morphometry and diffusivity

159 were found in various white and gray matter areas (**Figure 2-Supplement 1**). Together, these

160 data imply that expression of CMTM5 by oligodendrocytes is not essential for the normal

161 biogenesis, ultrastructure or protein composition of CNS myelin.

162

163 ***Cmtm5* deletion in oligodendrocytes causes early-onset progressive axonopathy and**

164 **late-onset general neuropathology**

165 Considering that the diameters of peripheral axons are increased when Schwann cells lack

166 CMTM6 (Eichel et al., 2020), we asked whether the diameters of CNS axons are altered when

167 oligodendrocytes lack CMTM5. Yet, the quantitative assessment of transmission electron

168 micrographs did not reveal abnormal axonal diameters in the optic nerves of cKO mice (**Figure**

169 **3-Supplement 1A,B**). Axonal diameters were also normal in mice lacking CMTM5 in all cells

170 (*Cmtm5$^{-/-}$*) compared to respective controls (**Figure 3-Supplement 1C**).

171

172 However, in the course of this analysis we noted a considerable number of pathological-

173 appearing axonal profiles. When quantifying these profiles at three different ages, we found

5

174   their frequency to increase over time in the optic nerves of *Cmtm5* cKO compared to control
175   mice (**Figure 3A,B**). Pathological profiles were evident in *Cmtm5* cKO optic nerves already at
176   P30, and their number progressively increased toward 1 year of age, the oldest analyzed
177   timepoint. We observed a trend toward a reduced number of axons in *Cmtm5* cKO mice at
178   P30 and P75 that reached significance at 1 year of age (**Figure 3C**). This implies that the
179   observed axonal pathology ultimately leads to axonal loss. To test whether *Cmtm5* cKO mice
180   display pathological profiles also in other white matter tracts, we used electron microscopy to
181   assess the dorsal white matter in spinal cords at 1 year of age. Indeed, the number of
182   pathological profiles was increased several-fold in *Cmtm5* cKO compared to control mice
183   (**Figure 3D,E**), indicating that the observed axonopathy is not restricted to the optic nerve.

184

185   We then used magnetic resonance spectroscopy (MRS) to determine the concentrations of
186   the metabolites myo-Inositol and N-Acetyl-Aspartate (NAA), which are considered
187   neuropathological markers reflecting gliosis and axonal degeneration respectively. We found
188   the concentrations of myo-Inositol significantly increased in the corpus callosi of *Cmtm5* cKO
189   compared to control mice at 8 months of age (**Figure 3-Supplement 2A**). *Cmtm5* cKO brains
190   displayed a trend toward reduced concentrations of NAA, which did not reach significance
191   (**Figure 3-Supplement 2B**). We considered that these findings may imply the emergence of
192   general neuropathology in the CNS of *Cmtm5* cKO mice, which we then aimed to resolve
193   temporally. To this aim we subjected the brains of *Cmtm5* cKO mice to immunohistochemistry
194   at the ages of P30, P75 and 1 year. We immunolabeled axonal swellings (using antibodies
195   against APP), astrocytes (using antibodies against GFAP) and microglia (using the markers
196   IBA1/AIF1 and MAC3/LAMP2). For quantification, we selected the hippocampal fimbria as a
197   relatively uniform white matter tract. At age P30 and P75 we found no genotype-dependent
198   differences between *Cmtm5* cKO and control mice with respect to number of APP-
199   immunopositive axonal swellings or the relative area of immunopositivity for GFAP, IBA1 or
200   MAC3. At one year of age, however, all markers were significantly increased in *Cmtm5* cKO
201   compared to control mice (**Figure 3-Supplement 3I-L**).

202

203   **Pathology of axon/myelin units by focused ion beam-scanning electron microscopy**
204   Considering that 2-dimensional visualization allows only limited insight into morphological
205   features, we next assessed pathological profiles in the optic nerves of one year old *Cmtm5*
206   cKO mice using 3-dimensional reconstruction of datasets gained by focused ion beam-
207   scanning electron microscopy (**Figure 4**). We found that the numbers of myelin outfoldings,
208   inner-tongue inclusions, and axoplasmic inclusions are not increased in *Cmtm5* cKO mice
209   (**Figure 4A´´-C´´**). Interestingly, however, the number of myelin whorls are markedly increased
210   in *Cmtm5* cKO mice (**Figure 4D´´**). Myelin whorls are multilamellar structures that largely

6

211   display the periodicity of CNS myelin devoid of a discernible axon, probably best interpreted

212   as remnants of degenerating myelinated fibers with relative sparing of myelin membranes

213   (Edgar et al., 2009). These data indicate that axonal degeneration - but not myelin pathology

214   such as myelin outfoldings or inner-tongue inclusions – emerges when oligodendrocytes lack

215   CMTM5.

216

217   **Functional assessment of retinae and optic nerves**

218   As a read-out for visual function, we first assessed retinal function by electroretinography

219   (ERG) recordings from *Cmtm5* cKO and control mice at 34 weeks of age. ERG waveforms

220   (**Figure 5A**), ERG thresholds (**Figure 5B**) and the amplitudes of the a- and b-waves (**Figure**

221   **5C,D**) did not differ between the genotypes, indicating normal retinal function. However,

222   visually evoked potentials (VEPs) implied that transmission of signals via the optic nerves to

223   the visual cortex was impaired in *Cmtm5* cKO mice (**Figure 5E-H**). All mice displayed sizeable

224   VEPs (**Figure 5E**) with normal thresholds (**Figure 5F**) and a normal VEP latency (**Figure 5G**),

225   indicating normal speed of action potential propagation and probably reflecting normal

226   myelination in the optic nerves. However, the VEP amplitudes were significantly reduced in

227   *Cmtm5* cKO mice (**Figure 5H**), probably owing to the axonopathy (**Figure 3, 4**).

228

229   **Axonopathy in constitutive and tamoxifen-induced *Cmtm5*-mutants**

230   All results presented thus far are based on the analysis of mice in which the *Cmtm5* allele was

231   recombined by Cre expressed in myelinating cells under control of the *Cnp* promoter.

232   Importantly, the utilized heterozygous $Cnp^{Cre/Wt}$ driver mice (Lappe-Siefke et al., 2003) harbor

233   only one functional *Cnp* allele. Notwithstanding that heterozygous $Cnp^{Cre/Wt}$ mice display

234   neuropathology only at old age (Hagemeyer et al., 2012), we sought to test if *Cmtm5* mutant

235   mice also display axonopathy on a homozygous wild-type *Cnp* gene background. To this aim

236   we bred mice carrying a homozygous deletion of the *Cmtm5* gene in all cells ($Cmtm5^{-/-}$, Knock-

237   out; $Cmtm5^{wt/wt}$, Control). As expected, CMTM5 was readily detectable by immunoblot in

238   myelin purified from the brains of control mice but undetectable in $Cmtm5^{-/-}$ myelin. Importantly,

239   the abundance of CNP appeared similar in $Cmtm5^{-/-}$ and $Cmtm5^{wt/wt}$ control myelin (**Figure**

240   **6A**), as was that of the myelin marker SIRT2. *Vice versa*, the abundance of CMTM5 appeared

241   similar by immunoblot analysis of purified from the brains of $Plp^{-/Y}$ and $Cnp^{-/-}$ and respective

242   control mice (**Figure 6-Supplement 1A,B**). Thus, the abundance of PLP and CNP in myelin

243   does not depend on CMTM5 and *vice versa* the abundance of CMTM5 in myelin does not

244   depend on PLP or CNP.

245

246   We then used conventional transmission electron microscopy to scrutinize optic nerves

247   dissected from $Cmtm5^{-/-}$ mice. Notably, by quantitative assessment of electron micrographs

248   we found a progressive increase in the number of pathological profiles in *Cmtm5^{-/-}* compared

249   to control mice (**Figure 6B,C**), in similarity to *Cmtm5* cKO mice (**Figure 3**). Importantly, this

250   indicates that the axonopathy that emerges when oligodendrocytes lack CMTM5 is

251   independent of *Cnp* heterozygosity.

252

253   To rule out that the pathological profiles in *Cmtm5* mutant mice are the consequence of subtle

254   developmental defects, we used the *Plp^{CreERT2}* driver line (Leone et al., 2003) to induce

255   recombination of the *Cmtm5* gene by injecting tamoxifen into adult *Cmtm5^{fl/fl}*Plp^{CreERT2}* mice

256   (termed *Cmtm5* iKO in the following). Tamoxifen injected *Cmtm5^{fl/fl}* mice served as controls.

257   By immunoblot, the abundance of CMTM5 was greatly reduced in myelin purified from the

258   brains of *Cmtm5* iKO mice four months after tamoxifen injection (4 mo PTI) (**Figure 6D**).

259   Importantly, by quantitative assessment of electron micrographs, *Cmtm5* iKO mice displayed

260   a significantly increased number of pathological profiles 4 mo PTI (**Figure 6E, F**). This indicates

261   that continued oligodendroglial expression of CMTM5 in adult mice is required to prevent the

262   emergence of axonopathy.

263

264   **Axonopathy upon *Cmtm5* deletion is counteracted by the Wallerian degeneration slow**

265   **(*Wld^s*) mutation**

266   To test if the axonopathy in *Cmtm5* mutants causes a decline in the number of neuronal cell

267   bodies, we quantified retinal ganglion cells (RGC) in the retinae of *Cmtm5* cKO and control

268   mice at 1 year of age (**Figure 7A-C**). We found that RGC numbers were similar, indicating that

269   neuronal cell bodies are preserved. Considering that this finding may imply a Wallerian-type

270   pathomechanism of axon degeneration (Coleman & Höke, 2020) we assessed if the presence

271   of the *Wld^s* mutation (Coleman et al., 1998; Lunn et al., 1989) affects the number of

272   pathological profiles upon *Cmtm5* deficiency. Indeed, when we analyzed the optic nerves of

273   *Cmtm5^{-/-}* mice by transmission electron microscopy (TEM) at the age of 6 months, presence

274   of the *Wld^s* mutation markedly reduced the number of pathological profiles (**Figure 7D-E**). For

275   comparison *Cmtm5^{wt/wt}* mice displayed only a negligible number of pathological profiles,

276   independent of the presence of the *Wld^s* mutation. Together, these results imply a Wallerian-

277   type pathomechanism of axonopathy when oligodendrocytes lack *Cmtm5*.

278

279

8

280 **Discussion**
281

282   We report the intriguing observation that mice lacking the CNS myelin protein CMTM5 display
283   an early-onset progressive axonopathy, whereas the biogenesis and ultrastructure of myelin
284   appear unaffected. According to previously established datasets, expression of *Cmtm5* in the
285   CNS is highly enriched in myelinating oligodendrocytes (Jäkel et al., 2019; Zhang et al., 2014;
286   Zhou et al., 2020). CMTM5 is not the first myelin protein associated with secondary axonal
287   degeneration in mutant mice. However, different from the previously studied myelin genes *Plp1*
288   (Edgar et al., 2004; Griffiths I et al., 1998; Lüders et al., 2019) and *Cnp* (Edgar et al., 2009;
289   Lappe-Siefke et al., 2003), the encoded protein is of much lower abundance in the myelin
290   sheath. By quantitative mass spectrometry, CMTM5 represents only 0.027% of the myelin
291   proteome (Jahn et al., 2020), in comparison to 37.9% for PLP and 5.1% for CNP. The relative
292   abundance of CMTM5 in myelin is thus roughly equivalent to that of other transmembrane-
293   tetraspan proteins CD9 (0.06%), proteolipid GPM6B (0.04%) and the gap junction protein
294   GJC3/Cx29 (0.02%) (Jahn et al., 2020), which were previously identified as low-abundant
295   myelin constituents (Kagawa et al., 1997; Kleopa et al., 2004; Werner et al., 2013). Considering
296   the low abundance of CMTM5 in myelin, it may not be unexpected that CMTM5-deficient mice
297   do not display primary ultrastructural defects that affect the myelin sheath when highly
298   abundant structural myelin proteins as PLP or CNP are lacking (**Table 1**). The comparison of
299   our different mouse mutants has revealed that CMTM5 is required by mature oligodendrocytes.
300   However, details of its mechanistic role in continued axon-glia interactions remain obscure.
301

302   CMTM5 is a member of the chemokine-like factor-like MARVEL-transmembrane containing
303   (CMTM) protein family (Han et al., 2003) that has been associated with regulating tumor
304   immunity (Burr et al., 2017; Mezzadra et al., 2017; Shao et al., 2007; Xiao et al., 2015; Yuan
305   et al., 2020), including CMTM5 itself. Comparatively little is known about the functional
306   relevance of CMTM proteins in the nervous system. However, we recently found the paralog
307   CMTM6 to be expressed in myelinating Schwann cells, in which it is involved in the previously
308   unknown function of Schwann cells to restrict the diameters of peripheral axons (Eichel et al.,
309   2020). The consequences of deleting CMTM5 and CMTM6 in oligodendrocytes and Schwann
310   cells, respectively, may appear roughly similar when considering that the myelin ultrastructure
311   is not affected while axonal features are altered. Notably, however, deleting CMTM6 from
312   Schwann cells causes increased diameters of peripheral axons but no signs of actual
313   degeneration (Eichel et al., 2020) whereas deleting CMTM5 from oligodendrocytes causes
314   CNS axonopathy without altering axonal calibers. Thus, CMTM5 and CMTM6 expressed by
315   oligodendrocytes and Schwann cells have distinct functions in the CNS and the PNS,
316   respectively.

9

317

318   The axonopathy observed upon deleting *Cmtm5* strongly implies that CMTM5 is involved in
319   the oligodendroglial function of preserving axonal integrity and that this function is not limited
320   to an early developmental stage. Oligodendroglial support of axons involves several
321   mechanisms, including supplying energy-rich substrates via monocarboxylate transporters
322   (Fünfschilling et al., 2012; Lee et al., 2012; Philips et al., 2021; Trevisiol et al., 2020), allocating
323   antioxidative proteins and other enzymes via extracellular vesicles (Chamberlain et al., 2021;
324   Frühbeis et al., 2020; Mukherjee et al., 2020), and modulating axonal transport (Edgar et al.,
325   2004; Frühbeis et al., 2020), these mechanisms being possibly interrelated. It will be an
326   important next step to identify the specific mechanism(s) of axonal support that are impaired
327   when oligodendrocytes lack CMTM5.

328

329   It is helpful to compare the pathology of previously described myelin mutants with the axonal
330   defects in CMTM5-deficient mice as assessed here. Notably, the presence of early-onset,
331   progressive axonopathy is a shared feature of the myelin mutant mice lacking PLP (Edgar et
332   al., 2004; Griffiths et al., 1998), CNP (Edgar et al., 2009; Lappe-Siefke et al., 2003) or CMTM5,
333   which are normally myelinated (*Cmtm5*-mutants) or display only moderate hypomyelination
334   (*Plp1* and *Cnp*-mutants). In contrast, entirely dysmyelinated *Mbp*-deficient *shiverer* mice
335   (Roach et al., 1985) do not display axonal degeneration (Griffiths I et al., 1998; Ou et al., 2009;
336   Uschkureit et al., 2000). This indicates that the lack of myelin *per se* is less detrimental for
337   axons than axonal ensheathment with functionally impaired myelin. Moreover, APP-
338   immunopositive axonal swellings, astrogliosis and microgliosis are early features when PLP
339   (Griffiths et al., 1998; de Monasterio-Schrader et al., 2013; Edgar et al., 2004; Steyer et al.,
340   2020; Trevisiol et al., 2020) or CNP (Edgar et al., 2009; Lappe-Siefke et al., 2003; Wieser et
341   al., 2013) are lacking, but emerges at much older age in CMTM5-deficient mice. This indicates
342   that the pathomechanisms differ between *Plp1* and *Cnp*-mutants and *Cmtm5*-mutants. This is
343   supported by our observation that the axonopathy is ameliorated by the presence of the *Wld^s*
344   mutation in CMTM5-deficient mice, different form that in PLP- and CNP-deficient mice, at least
345   at the examined time points and in presence of one copy of the *Wld^s* gene (Edgar et al., 2004,
346   2009). Together, this implies different dynamics, and probably different mechanisms of
347   axonopathy when oligodendrocytes lack PLP, CNP or CMTM5.

348

349   The *Wlds* mutation can protect axons from various types of physical, toxic or genetic insult
350   (Coleman et al., 1998; Coleman & Höke, 2020; Lunn et al., 1989). In the *Wld^s* pathway, a key
351   regulator of axonal degeneration is the enzyme sterile alpha and TIR motif containing protein
352   1 (SARM1) (Gerdts et al., 2013; Osterloh et al., 2012). Both, the *Wld^s* mutation and deletion of
353   the *Sarm1* gene can delay axonal degeneration (Coleman et al., 1998; Hopkins et al., 2021),

354   involving the maintenance of high NAD$^+$ levels along the axon (di Stefano et al., 2015; Gilley

355   & Coleman, 2010; Hopkins et al., 2021; Wang et al., 2005).To the best of our knowledge,

356   CMTM5-deficient mice represent the first model in which the axonopathy that emerges upon

357   deletion of a CNS myelin protein is ameliorated by the *Wld^s* mutation. Only the degeneration

358   of axons in the PNS of mice lacking myelin protein zero (MPZ/P0) is robustly delayed by the

359   presence of the *Wld^s* mutation (Samsam et al., 2003). Thus, genetic defects of

360   oligodendrocytes or Schwann cells can cause an axonopathy with a Wallerian-like

361   pathomechanism in the CNS and PNS, respectively. It will be important to test if the currently

362   developed small molecule SARM1 inhibitors (Bosanac et al., 2021; Hughes et al., 2021; Loring

363   et al., 2020) allow counteracting axonal degeneration secondary to an insult primarily affecting

364   oligodendrocytes.

365

366

Material and Methods

Mouse models and mouse lines

Frozen sperm of mice carrying the 'knockout-first' allele of the *Cmtm5* gene (C57BL/6N-A[tm1Brd] *Cmtm5[tm1a(KOMP)Wtsi]/Wtsi*) was acquired from The Mouse Genetics Project (Wellcome Trust Sanger Institute, Hinxton, UK). *Cmtm5[tm1a(KOMP)Wtsi]* mice were generated by the transgene facility of the Max Planck Institute of Experimental Medicine (Göttingen, Germany) by *in vitro* fertilization using standard procedures. The LacZ/neo cassette was deleted by crossbreeding these mice with *Gt(ROSA)26Sor[tm1(FLP1)Dym]* mice expressing flippase (Farley et al., 2000) yielding mice heterozygous for the floxed *Cmtm5* allele (*Cmtm5[tm1c(KOMP)Wtsi]* mice, also termed *Cmtm5^{fl/+}*) which were bred to homozygosity. To delete *Cmtm5* in oligodendrocytes, *Cmtm5^{fl/fl}* mice were crossbred with mice expressing *Cre* under the *Cnp* promoter (*Cnp1[tm(cre puro)Kan]* mice, also termed *Cnp[Cre/WT]*; Lappe-Siefke et al., 2003) yielding *Cmtm5^{fl/fl}*Cnp[Cre/WT]* mice (also termed *Cmtm5* cKO). In experiments assessing *Cmtm5* cKO mice, *Cmtm5^{fl/fl}* mice served as controls. Taking advantage of germline-recombination we gained a mouse line with a body-wide deletion of *Cmtm5* (*Cmtm5[tm1d(KOMP)Wtsi]* mice, also termed *Cmtm5^{-/-}* or Knock-out). In experiments assessing *Cmtm5^{-/-}* mice, *Cmtm5^{+/+}* mice served as controls. To delete *Cmtm5* in oligodendrocytes of adult mice, *Cmtm5^{fl/fl}* were crossbred with mice expressing tamoxifen-inducible *Cre* under the *Plp* promoter (Tg(Plp1-cre/ERT2)1Ueli, *Plp[CreERT2]*,Leone et al., 2003) resulting in *Cmtm5^{fl/fl}* Plp[CreERT2]* mice (also termed *Cmtm5* iKO) and respective controls without *Cre.* For induction, male mutant mice (*Cmtm5^{fl/fl}* Plp[CreERT2]*) and male control mice (*Cmtm5^{fl/fl}*) were injected with Tamoxifen intraperitoneally at 8 weeks of age for 10 days with a 2-day break after the first five injection days (1 mg tamoxifen dissolved in 100 µl corn oil per mouse and day). *Cmtm5^{+/-}* mice were crossbred with *Cmtm5^{+/-}* mice harboring the *WLD[S]* mutation (Wld[s], Coleman et al., 1998; Mack et al., 2001) to obtain all experimental groups from the same breeding scheme (Control groups: *Cmtm5^{+/+}* and *Cmtm5^{+/+}*Wld[s]*; knock-out groups: *Cmtm5^{-/-}* and *Cmtm5^{-/-}*Wld[s]*). Littermate mice were used as experimental controls as far as possible.

Genotyping was carried out by genomic PCR. *Cmtm5* genotypes were assessed with the same PCR strategy in all *Cmtm5* lines (*Cmtm5* cKO, *Cmtm5^{-/-}*, *Cmtm5* iKO, *Cmtm5*Wld[s]*). Sense primer (5`-AGTAGTGGCC CATTGCCATC) in combination with antisense primer (5`-TGGTTAGGGG GCTCCTCTTC) yielded a 626 bp product (floxed allele) or 437 bp product (wildtype). In the same reaction, antisense primer (5`-GAGCTCAGAC CATAACTTCG) was used to detect *Cmtm5* allele recombination yielding a 313 bp fragment. Detection of the *Cnp[Cre]* allele (Lappe-Siefke et al., 2003) was carried out using sense primer (5'-GCCTTCAAAC TGTCCATCTC) and antisense primer (5'-CCCAGCCCTT TTATTACCAC) amplifying a 700 bp product. As well as a sense (5'-CAGGGTGTTA TAAGCAATCCC) and antisense (5'-

12

404 CCTGGAAAAT GCTTCTGTCCG) primer yielding a 357bp fragment when Cre positive.

405 *Plp*^{*CreERT2*} (Leone et al., 2003)was detected using sense primer (5`-TGGACAGCTG

406 GGACAAAGTAAGC) and antisense primer (5`-CGTTGCATCG ACCGGTAATGCAGGC)

407 yielding a 250 bp product. The *Wlds* mutation (Coleman et al., 1998; Mack et al., 2001) was

408 detected using sense primer (5`-CGTTGGCTCT AAGGACAGCAC) and antisense primer (5`-

409 CTGCAGCCCC CACCCCTT) yielding a 182 bp product.

410

411 Mice were bred and kept in the mouse facility of the Max Planck Institute of Experimental

412 Medicine, Göttingen. Experimental mutant mice were analyzed with littermate controls as far

413 as possible. All animal experiments were performed in accordance with the German animal

414 protection law (TierSchG) and approved by the Niedersächsisches Landesamt für

415 Verbraucherschutz und Lebensmittelsicherheit (LAVES) under license 33.19-42502-04-

416 15/1833 and 33.8-42502-04-19/3172.

417

Biochemical purification of myelin from mouse brains

419 Purification of a myelin-enriched light weight membrane fraction from nervous tissue using

420 sucrose density centrifugation and osmotic shocks was previously described (Erwig, Patzig, et

421 al., 2019). Mice were sacrificed by cervical dislocation. Protein concentrations of brain lysate

422 and myelin fractions were determined using the DC Protein Assay Kit (Bio-Rad, Munich,

423 Germany) following the manufacturer´s instruction and measured using the Eon^{TM} High

424 Performance Microplate Spectrophotometer (BioTek, Vermont, USA).

425

Immunoblotting

427 Immunoblotting was essentially performed as described (Schardt et al., 2009). Brain lysate

428 and myelin fraction samples were diluted in 4x SDS sample buffer (Glycerol 40% [w/v], Tris/HCl

429 pH 6.8 240mM, sodium dodecyl sulfate (SDS) 8% [w/v] Bromphenol blue 0.04% [w/v]; 5%

430 Dithiothreitol (DTT) was added as a reducing agent. Before usage, samples were heated at

431 40°C for 10 min. For protein separation by SDS-PAGE, the Mini-PROTEAN Handcast system

432 (BioRad, Munich, Germany) was used with self-casted acrylamide gels (10-15%). 5-15 µg

433 samples were loaded per well (depending on protein of interest) next to 5 µl pre-stained protein

434 ladder (PageRuler^{TM}, ThermoFischer Scientific, Waltham, USA). Proteins were separated by

435 constant current (200V) for 45-60 min using a BioRad power supply. Immunoblotting was

436 carried out with a Novex® Semi-Dry Blotter (Invitrogen, Karlsruhe, Germany) and proteins

437 were transferred to an activated (100% Ethanol, 1 min; followed by two washing steps with

438 water) PVDF membrane (GE Healthcare, Buckinghamshire, UK; Cat# 10600023) at 20V for

439 45 min. After blotting, membranes were blocked in 1xTBS containing 5% non-fat dry milk

440 (Frema, Karlsruhe, Germany) and 0.05% Tween-20 for one hour at room temperature (RT).

441 Primary antibodies were diluted in 5 ml blocking buffer and incubated overnight at 4°C and

442 horizontal rotation. Membranes were washed thrice with TBS-T for 5-10 min each and

443 incubated for one hour with secondary HRP antibodies diluted in blocking buffer. Membranes

444 were washed three times with TBS-T for 5-10 min. Detection was carried out using enhanced

445 chemiluminescent detection (ECL) according to the manufacturer´s instructions (Western

446 Lightning® Plus-ECL or SUperSignal[TM] West Femto Maximum Sensitive Substrate; Thermo

447 Fischer Scientific, St Leon-Rot, Germany). Immunoblots were scanned using ECL Chemostar

448 (Intas Science Imaging, Göttingen, Germany). For antibody information see **Table 2**.

449

450 **Label-free quantification of myelin proteins**

451 In-solution digestion of myelin proteins according to an automated filter-aided sample

452 preparation (FASP) protocol (Patzig et al., 2016) and LC-MS-analysis by different MS[E]-type

453 data-independent acquisition (DIA) mass spectrometry approaches was performed as recently

454 established for PNS (Siems et al., 2020) and CNS (Jahn et al., 2020) myelin. Briefly, protein

455 fractions corresponding to 10 µg myelin protein were dissolved in lysis buffer (1% ASB-14, 7

456 M urea, 2 M thiourea, 10 mM DTT, 0.1 M Tris pH 8.5) and processed according to a CHAPS-

457 based FASP protocol in centrifugal filter units (30 kDa MWCO, Merck Millipore). After removal

458 of the detergents, protein alkylation with iodoacetamide, and buffer exchange to digestion

459 buffer (50 mM ammonium bicarbonate (ABC), 10 % acetonitrile), proteins were digested

460 overnight at 37°C with 400 ng trypsin. Tryptic peptides were recovered by centrifugation and

461 extracted with 40 µl of 50 mM ABC and 40 µl of 1% trifluoroacetic acid (TFA), respectively.

462 Combined flow-throughs were directly subjected to LC-MS-analysis. For quantification

463 according to the TOP3 approach (Silva et al., 2006), aliquots were spiked with 10 fmol/µl of

464 Hi3 EColi standard (Waters Corporation), containing a set of quantified synthetic peptides

465 derived from E. coli. Chaperone protein ClpB.

466

467 Nanoscale reversed-phase UPLC separation of tryptic peptides was performed with a

468 nanoAcquity UPLC system equipped with a Symmetry C18 5 µm, 180 µm × 20 mm trap column

469 and a HSS T3 C18 1.8 µm, 75 µm × 250 mm analytical column (Waters Corporation)

470 maintained at 45°C. Peptides were separated over 120 min at a flow rate of 300 nl/min with a

471 gradient comprising two linear steps of 3-35% mobile phase B (acetonitrile containing 0.1%

472 formic acid) in 105 min and 35-60% mobile phase B in 15 min, respectively. Mass

473 spectrometric analysis on a quadrupole time-of-flight mass spectrometer with ion mobility

474 option (Synapt G2-S, Waters Corporation) was performed in the dynamic range-enhanced

475 (DRE)-UDMS[E] mode as established previously for proteome analysis of purified myelin (Jahn

476 et al., 2020; Siems et al., 2020). Continuum LC-MS data were processed using Waters

477 ProteinLynx Global Server (PLGS) and searched against a custom database compiled by

14

478 adding the sequence information for E. coli. Chaperone protein ClpB and porcine trypsin to the

479 UniProtKB/Swiss-Prot mouse proteome (release 2017-07, 16909 entries) and by appending

480 the reversed sequence of each entry to enable the determination of false discovery rate (FDR).

481 Precursor and fragment ion mass tolerances were automatically determined by PLGS and

482 were typically below 5 ppm for precursor ions and below 10 ppm (root mean square) for

483 fragment ions. Carbamidomethylation of cysteine was specified as fixed and oxidation of

484 methionine as variable modification. One missed trypsin cleavage was allowed. Minimal ion

485 matching requirements were two fragments per peptide, five fragments per protein, and one

486 peptide per protein. The FDR for protein identification was set to 1% threshold.

487

488 For post-identification analysis including TOP3 quantification of proteins, ISOQuant (Distler et

489 al., 2014; Kuharev et al., 2015) software freely available at www.isoquant.net) was used as

490 described previously (Jahn et al., 2020; Siems et al., 2020). Only proteins represented by at

491 least two peptides (minimum length six amino acids, score ≥ 5.5, identified in at least two runs)

492 were quantified as parts per million (ppm), i.e. the relative amount (w/w) of each protein in

493 respect to the sum over all detected proteins. FDR for both peptides and proteins was set to

494 1% threshold and at least one unique peptide was required. Proteome profiling comparing

495 myelin from *Cmtm5* cKO and CTRL mice was performed with three biological replicates and

496 duplicate digestion, resulting in a total of 6 LC-MS runs per condition. The mass spectrometry

497 proteomics data have been deposited to the ProteomeXchange Consortium via the PRIDE

498 (Perez-Riverol et al., 2019) partner repository with dataset identifier **PXD029443**.

499

500 **Electron microscopy**

501 For transmission electron microscopy (TEM) optic nerves and spinal cords were dissected and

502 fixed in Karlsson-Schulz fixative (4% PFA, 2.5% Glutaraldehyde in 0.1 M phosphate buffer)

503 overnight. Samples were processed and embedded in epoxy resin (Serva, Heidelberg,

504 Germany) as described (Möbius et al., 2010). For TEM, ultrathin (50 nm) sections were

505 prepared using a PTPC Powertome Ultramicrotome (RMC, Tuscon Arizona, USA) and a

506 diamond knife (Diatome AG, Biel, Switzerland). Sections were cut and collected on formwar

507 coated copper grids (AGAR scientific, Essex, UK). To enhance contrast, ultrathin sections

508 were stained with UranyLess (Electron Microscopy Science, Hatfield, Panama) for 20 min and

509 washed 6 times with $_{dd}H_2O$. For analysis 16-20 non-overlapping random images were taken

510 per animal using the Zeiss EM900 at 7000x (one image = 220 μm^2). All image analysis was

511 performed using Fiji (Version 2.0.0-rc-68/1.52i; Schindelin et al., 2012).

512

513 To assess relative number of pathological axons (degenerated axons, axonal swellings) and

514 pathological myelin (myelin outfoldings, double myelination, inner tongue swelings) units, all

515 axons on 16-20 non-overlapping random images were analyzed per mouse. For axon diameter
516 analysis, all normal-appearing, accurately cross-sectioned myelinated axons were evaluated
517 on 16-20 non-overlapping random images. Data is presented as mean axonal diameter per
518 animal. g-ratios were calculated as ratio between axonal diameter and the outer diameter of
519 the corresponding myelin sheath. In total 180-200 axons were randomly selected for g-ratio
520 analysis from 16-20 EM images per mouse using the Fiji Grid tool (Circular grids, 3 μm^2 per
521 point, random offset).

522

523 For the analysis of axon number, semithin sections (thickness 500 nm) were cut and stained
524 with methylene blue/azur II (1:1) for one minute followed by a washing step with H_2O. Images
525 were acquired at 100x using a bright-field light microscope (Zeiss AxioImager Z1 coupled to a
526 Zeiss Axio Cam MRc camera; controlled and stitched by Zeiss Zen 1.0 software). Using Fiji,
527 optic nerve images were separated into 55 μm^2 rectangles. From all rectangles filled with ON
528 tissue 5 were chosen at random and all axons were counted. Axon number is shown as mean
529 of 5 assessed rectangles per mouse.

530

531 **Focused ion beam – scanning electron microscopy**
532 Samples were prepared according to (Steyer et al., 2020). In brief, dissected optic nerve
533 samples were immersed in primary fixative (Karlsson-Schultz phosphate buffer: 109.5 mM
534 $NaH_2PO_4 \cdot H_2O$, 93.75 mM $Na_2HPO_4 \cdot 2H_2O$, 86.2 mM NaCl, 2.5% glutaraldehyde, 4%
535 formaldehyde. Adjust the pH to 7.4 and filter, at 4 °C for at least 24 h) and processed with a
536 modified OTO-protocol (osmium-thiocarbohydrazide-osmium) as previously described (Weil
537 et al., 2018) based on a previously established original protocol (Deerinck et al., 2010). Briefly,
538 samples were post-fixed for 3 h with 2% OsO_4 (EMS, Hatfield, USA) and 1.5% $K_3Fe(CN)_6$
539 (EMS, Hatfield, USA) at 4°C followed by a contrasting step with 1% thiocarbohydrazide
540 (Sigma-Aldrich, St. Louis, USA) for 1 h at room temperature and 1.5 h incubation with 2%
541 OsO_4. *En bloc* staining was performed with 2% uranyl acetate overnight at 4°C. The next day
542 the samples were dehydrated through a series of ascending concentrations of acetone (EMS,
543 Hatfield, USA) for 15 min each (30%, 50%, 75%, 90%, 3× 100%) and incubated with increasing
544 concentrations of the epoxy resin Durcupan (Sigma-Aldrich, St. Louis, USA) (2:1, 1:1, 1:2) for
545 2 h each and left over night in 90% Durcupan without component D. The next day the samples
546 were incubated with 100% Durcupan (all components: A (epoxy resin) 11.4 g, B (hardener) 10
547 g, C (accelerator) 0.3 g, D (plasticizer) 0.1 g) for 4.5 h and polymerized for 48 h at 60°C.

548

549 The polymerized samples were trimmed using a 90° trimming knife (Diatome AG, Biel,
550 Switzerland) and positioned on a SEM-stub using silver conductive resin (EPO-TEK 129-4)
551 (EMS, Hatfield, USA). The surface was sputter coated (Leica, ACE 600) (Leica, Wetzlar,

552 Germany) with a layer of 10 nm platinum and placed inside the FIB-SEM (Crossbeam 540,
553 Zeiss, Oberkochen, Germany). After exposing a cross-section through the region of interest
554 with 15 nA ion current and polishing with 7 nA, a 400 nm deposition of platinum was performed
555 using 3 nA. The final dataset was acquired at 1.5 kV (1000 pA) 5 nm × 5 nm × 25 nm voxel
556 size with a milling current of 1.5 nA. Fiji (Schindelin et al., 2012) was used for all following
557 image processing steps: The images were aligned using the SIFT algorithm, cropped and
558 inverted. They were smoothed using a Gaussian blur (sigma 1) and a local contrast
559 enhancement was applied (CLAHE: blocksize 127, histogram bins 256, maximum slope 1.25).
560 The dataset was binned by 2 in x and y. Analysis of pathological myelin and axon profiles was
561 carried out using Fiji. All profiles in the volume belonging to one of the categories (myelin
562 outfoldings, inner-tongue inclusions, axoplasmic inclusions, myelin whorls) were counted, and
563 values were normalized to a volume of 10000 μm^3. Example 3D models were reconstructed
564 using IMOD (v 4.9.12, University of Colorado, https://bio3d.colorado.edu/imod).

565

566 **Immunohistochemistry**
567 Sections (5 μm) of paraffin-embedded brains were used to determine neuropathology and
568 oligodendrocyte number. Section preparation was as previously described (de Monasterio-
569 Schrader et al., 2012; Patzig et al., 2016). To assess neuropathology in *Cmtm5* cKO and
570 control mice, 3-5 mice per genotype were analyzed for each timepoint (P30, P75, P365) and
571 labelled for amyloid precursor protein (APP) (Chemicon, 1:1000), MAC3 (Pharmingen, 1:400),
572 glial fibrillary acidic protein (GFAP) (Novo Castra, 1:200) or IBA1 (abcam, 1:1000). Images
573 were acquired at 40x magnification using a bright-field light microscope (Zeiss AxioImager Z1,
574 coupled to Zeiss AxioCam MRc Camera; controlled and stitched by Zeiss Zen 1.0 software).
575 The hippocampal fimbria was analyzed by counting APP positive axonal swellings per selected
576 area or by using an ImageJ plugin to semiautomatically determine the area of
577 GFAP/MAC3/IBA1 immunopositivity as previously described (de Monasterio-Schrader et al.,
578 2012; Lüders et al., 2017; Patzig et al., 2016). To assess oligodendrocyte number, sections of
579 paraffin-embedded brains from *Cmtm5* cKO and control mice at P75 were deparaffinized and
580 rehydrated as with sections for neuropathology. Sections were then blocked for 1 hour at room
581 temperature with PBS containing BSA and horse serum. Incubation with primary antibody was
582 then carried out over 48h at 4°C with anti-CAII antibody (1:300 in PBS containig 1% HS). Slides
583 were washed thrice for 10 minutes with PBS and incubated with DAPI (Thermo Scientific,
584 Waltham, USA) and anti-rabbit Alexa555 (Dianova, 1:1000 in PBS containing 1% HS). Slides
585 were washed again thrice with PBS for 10 minutes and mounted using AquaPolymount. The
586 hippocampal fimbria was imaged using the Axio Observer Z2 (Zeiss) at a 40x magnification
587 and stitched using Zeiss Zen2011. All cells positive for both DAPI and CAII were identified as

588 oligodendrocytes. All positive cells were counted and normalized to an area of 1 mm^2. For
589 antibody information see **Table 2**.

590

591 **Preparation of cryosections and confocal imaging**
592 Cryosection were obtained from spinal cords immersion fixed with 4% PFA overnight. Nerves
593 were then transferred to a sucrose buffer (10% [w/v], 20% [w/v], 30% [w/v] in 0.1 M phosphate
594 buffer) over night at 4°C for each concentration. The nerves were then embedded in small
595 plastic chambers using Tissue-Tek® O.C.T.^{TM} Compound (Sakura, Staufen, Germany).
596 Nerves were stored at -20°C until further use. 10 µm thick cross-sections were prepared using
597 a cryostat (Reichert Jung® Cryocut 18000, Wetzlar, Germany) and transferred to Superfrost®
598 Plus microscope slides (Thermo Fischer Scientific, St. Leon-Rot, Germany). Slides were dried
599 for 30 minutes at room temperature and stored at -20°C until further use.

600

601 Sections were stained with the following protocol using 200 µl volumes per slide: 3 minutes
602 Methanol, 30 minutes permeabilization using PBS with 0.4% [v/v] Triton-X100 (Sigma Aldrich,
603 St. Louis, USA) followed by blocking using DAKO blocking buffer (DAKO, Hamburg, Germany)
604 for 60 minutes. TUJ1 (Covance) and CMTM5 (custom made by Pineda, Berlin, Germany Table
605 2) antibodies were diluted in antibody diluent (DAKO, Hamburg, Germany) and incubated for
606 48 hours at 4°C in a dark, humid chamber. Sections were then washed three times with PBS
607 for 10 minutes and incubated with secondary antibodies (α-rabbit STAR-RED, α-mouse STAR-
608 ORANGE, abberior, Göttingen, Germany, Table 2) diluted 1:200 in antibody diluent for 60
609 minutes. Sections were washed 3 times with PBS for 10 minutes and mounted using
610 AquaPolymount (Polysciences, Warrington, USA). Images were obtained on a Confocal and
611 STED FACILITY line microscope (Abberior Instruments, Germany) and acquired as xy-plane
612 with a pixel size of 30nm. The fluorophores were excited with appropriate excitation lasers at
613 640nm (abberior STAR RED) and 561nm (abberior STAR ORANGE). For image acquisition
614 the microscope software "Lightbox" as provided by Abberior Instruments was used.

615

616 **Magnetic Resonance Imaging and Spectroscopy**
617 Magnetic resonance imaging (MRI) and spectroscopy (MRS) were acquired on a 9.4T Bruker
618 BioSpec MR system with a 30 cm horizontal bore and B-GA12 gradient system operating on
619 Bruker ParaVision 6.0.1 (Hardware and software from Bruker BioSpin MRI GmbH, Ettlingen,
620 Germany). A four-channel (2×2) receive-only mouse head coil was used, in combination with
621 a 112/84 resonator, to acquire MRI and MRS (both from Bruker BioSpin MRI GmbH, Ettlingen).

622

623 The MRI protocol included magnetization transfer (MT)-weighted images and diffusion-
624 weighted images. For MT, a 3D fast low angle shot (FLASH) sequence was used to acquire

18

625 three datasets: MT-weighted, proton density-weighted, and T1-weighted (repetition time [15.1,

626 15.1, 18] ms, echo time 3.4 ms, flip angles [5˚, 5˚, 25˚], two averages, voxel size 100 μm × 100

627 μm × 100 μm, acquisition time 18.4 min). These datasets were used to estimate MT saturation

628 (MTsat) according to the method described by (Helms et al., 2008). Diffusion-weighted images

629 (DWI) were acquired using a spin-echo echo-planar imaging sequence (repetition time 2000

630 ms, echo time 21.5 ms, two repetitions, voxel size 100 μm × 100 μm × 500 μm, gradient

631 duration and separation 2.5 ms and 12.5 ms, b values 0, 1000 and 2000, gradient directions

632 30 for each b value, acquisition time 17.2 min). These DWI were preprocessed through

633 denoising (Fadnavis et al., 2020) and averaged across repetitions. A diffusion tensor model

634 (Basser et al., 1994) was fitted to the preprocessed DWI data, and fractional anisotropy (FA),

635 axial diffusivity (AD), radial diffusivity (RD), and mean diffusivity (MD) maps were derived

636 (Garyfallidis et al., 2014). Multi-echo gradient-recalled echo (GRE) images were acquired

637 using a 3D GRE sequence (repetition time 25 ms, echo time 2.2 ms, echo spacing 2 ms,

638 number of echoes 10, flip angle 12˚, four averages, voxel size 70 μm × 70 μm × 300 μm,

639 acquisition time 19 min). The effective transverse relaxation rate (R_2^*) maps were calculated

640 using by fitting the multi-echo GRE magnitude signal decay across all echo times with a mono-

641 exponential model (Pei et al., 2015).

642

643 MRS was acquired from cortices and corpus callosi using a stimulated echo acquisition mode

644 (STEAM) sequence. The parameters of the STEAM sequence were: repetition time of 6000

645 ms, echo time of 10 ms, spectral width of 5000 Hz, 2048 data points, 128 averages, and a total

646 acquisition time of 12:48 min. The dimensions of the cortical and corpus callosal voxels were

647 $3.9×0.7×3.2$ mm^3 and $3.9×0.7×1.7$ mm^3, respectively. All spectra were acquired with CHESS

648 water suppression and outer volume suppression. The spectra were analyzed and quantified

649 using LCModel (Provencher, 1993) in the chemical shift range from 0.2 to 4.2 ppm. Values

650 with Cramer-Rao lower bounds above 20% were excluded from further analyses. Statistics

651 were performed in *Excel* using a 2-tailed, unpaired Student´s t-test assuming equal variance.

652

653 **Electroretinography (ERG) and visually evoked potentials (VEP)**

654 ERGs were recorded as described (Dieck et al., 2012) and VEP were recorded essentially as

655 described (Ridder & Nusinowitz, 2006). Briefly, mice were dark adapted overnight and

656 anesthetized with Ketamin (125μg/g), Xylazin (2,5μg/g) and Buprenorphin i.p. (0,1 mg/kg).

657 Eyes were kept moist using contact lens solution containing hyaluronic acid for ERG recordings

658 and with Methocel (DuPont Pharma, Mississauga, Canada) for VEP recordings. For ERG

659 recordings, a silver ball electrode placed in the outer angle of the left eye served as active

660 electrode. Signals were averaged 10 times. For VEP recordings, the scalp was resected and

661 a small hole was drilled on the right side 1 mm lateral and 1mm rostral of lambda and a thin

19

662 needle electrode was inserted superficially. Signals were averaged at least 50 times. The
663 reference electrode was placed on the nose of the mouse and the common ground near the
664 hind legs. Signals were amplified 1000 times (NeuroAmp) and sampled without analog filtering.
665 0.1 ms light flashes were generated using BioSig Software and TDT system III hardware
666 (Tucker Davis Technologies, Davis, USA) and presented via a custom-designed Ganzfeld
667 apparatus at a stimulus rate of 0.5 Hz. Illumination was calibrated using a luxmeter (Mavolux
668 5032c, Nürnberg, Germany) and an Integrated Photodiode Amplifier 10530 (Integrated
669 Photomatrix Limited, Dorchester, UK). Analysis was performed using custom written matlab
670 scripts (version 2019b). For analysis of ERG and VEP thresholds, Student´s t-test was applied.
671 Data from ERG and VEP analysis (**Figure 5**) is represented in line graphs showing mean
672 values of mice per genotype ±SEM. To determine the genotype-dependent effect on ERG and
673 VEP amplitude and latencies across various light intensities, 2-way-ANOVA was applied.
674

Retina preparation and assessment of retinal ganglion cell number

676 To assess retinal ganglion cell numbers (RGC), eyes of 1 year old *Cmtm5$^{-/-}$* mice and
677 respective controls were dissected and fixed for one hour with 4% PFA/Phosphate Buffer (PB).
678 Eyes were then rinsed in PB and retinae were dissected as follows. The eye was cut open
679 along the ciliary body and cornea and lens were removed. The retinal pigment epithelium
680 (RPG) was carefully removed. Four cuts on opposing sites were made to flatten the retina. The
681 retina was transferred into a 24 well plate with 1 retina per well containing PBS. Retinae were
682 washed with PBS/2% Triton X-100 (500 µl/well) at room temperature and gentle agitation for
683 10 minutes. To permeate nuclear membranes the wash solution was replaced by fresh
684 PBS/2% Triton X-100 and retinae were frozen at -80°C for 10 minutes. Retinae were washed
685 twice with PBS/0.5% Triton X-100 for 5 minutes at room temperature. To reduce unspecific AB
686 binding retinae were incubated with blocking buffer (PBS/ 5%BSA/ 5% Donkey Serum/ 2%
687 Triton X-100) for 1 hour at room temperature with gently agitation. To label RGCs, retinae were
688 incubated with guinea pig anti-RBPMS (Sigma-Aldrich, St. Louis, USA); 1:200 in blocking
689 buffer, 350 µl per well) for 2 hours at room temperature. Retinae were then washed thrice with
690 PBS/0.5% Triton X-100 for 10 minutes at RT. RGCs were labelled using donkey anti-guinea
691 pig Alexa 555 (1:1000 in blocking buffer) and incubated over night at 4°C. Retinae were then
692 washed thrice for 30 minutes with PBS and transferred to a superfrost slide with a fine brush.
693 Retinae were mounted using AquaPolymount with the RGC layer facing up. Slides were kept
694 at 4°C and dark until imaging. Images were taken using the Axio Observer Z2 (Zeiss) and a
695 40x magnification and stitched using Zeiss Zen2011. For assessment of RGC number the
696 average of 3 different areas (area= mm^2 per rectangle) were analyzed for each part of the
697 retina (inner/middle/outer). Retinae of three individual mice per genotype were analyzed.
698

Statistics

All experiments were analyzed blinded to genotypes. Statistical assessment was performed using GraphPad Prism 8 (GraphPad Software Inc., San Diego, United States) unless noted otherwise. Two-sided Student´s t-test was used to compare two groups unless specified otherwise. Welch´s correction was performed in case of unequal distribution. Levels of significance were set as $p<0.05$ (*), $p<0.01$ (**) and $p< 0.001$ (***). Exact p-values are given in the figure legends, except those for the MRI data in **Figure 2 Supplement 1** are listed below. For all experiments, statistical test used and correction are given in the figure legend. Data in **Figure 1 Supplement 1**; **Figure 2 D-E, I-J, N**; **Figure 3 B, C, E**; **Figure 3 Supplement 1**; **Figure 3 Supplement 2**; **Figure 3 Supplement 3**, **Figure 4 A``-D``**; **Figure 6 C, F**; **Figure 7 C, E**; are given as bar graphs with mean ±SEM; data points represent individual mice. Data from MRI analysis (**Figure 2 Supplement 1**) and ERG and VEP thresholds (**Figure 5 B, F**) are presented as boxplots; data points represent individual mice. Data for frequency distribution of axonal diameters (**Figure 3-Supplement 1 A´-C´**) are presented as bar graphs showing binned axonal diameters pooled of all mice per condition. Proteome data (**Figure 2 B,B´**) is presented as volcano plot and heat map. Data correspond to 3 mice per genotype and 2 technical replicate per mouse. The Bioconductor R packages 'limma' and 'q-value' were used to detect significant changes in protein abundance by moderated t-statistics as described (Ambrozkiewicz et al., 2018; Siems et al., 2020). Further information is provided in **Figure 2B source data 1**. g-ratios (**Figure 2 G, L**) are presented as scatter plots. Each data point represents an individual axon. In total, 200 axons were analyzed per mouse and 5 mice were analyzed per genotype. Data from ERG and VEP analysis (**Figure 5**) is represented in line graphs showing mean values of mice per genotype ±SEM. To determine the genotype-dependent effect on ERG and VEP amplitude and latencies across light intensities, 2-way-ANOVA was applied.

Exact sample size and number of mice are given in the figures or in the figure legends, except for the significance levels for MRI data in **Figure 2 supplement 1** which were as follows. CC, Corpus callosum; Fim, Fimbria; Thal, Thalamus; Cort, Cortex; AC, Anterior commissure. Two-sided Student´s t-test was applied. **(B)** CC: p= 0.1739; Fim: p= 0.2244; Thal: p= 0.3229; Cort: p= 0.6159; AC: p= 0.3290. **(C)** CC: p= 0.7263; Fim: p= 0.2223; Thal: p= 0.9943; Cort: p= 0.5009; AC: p= 0.2425. **(D)** CC: p= 0.7103; Fim: p= 0.2608; Thal: p= 0.6903; Cort: p= 0.3576; AC: p= 0.2531. **(E)** CC: p= 0.4374; Fim: p= 0.2038; Thal: p= 0.8343; Cort: p= 0.5728; AC: p= 0.2678. **(F)** CC: p= 0.7065; Fim: p= 0.8432; Thal: p= 0.7319; Cort: p= 0.8614; AC: p= 0.9983.

Data availability statement

The mass spectrometry proteomics data have been deposited to the ProteomeXchange Consortium via the PRIDE partner repository with dataset identifier **PXD029443**.

Ethics Statement

All animal experiments were performed in accordance with the German animal protection law (TierSchG). Ethical review of animal experiments was performed by the Niedersächsisches Landesamt für Verbraucherschutz und Lebensmittelsicherheit (LAVES) and approved with licenses 33.19-42502-04-15/1833 and 33.8-42502-04-19/3172.

Competing interest statement

MM is affiliated with Abberior Instruments Gmbh; the author has no financial interests to declare. KAN is a Reviewing Editor for eLIFE. All other authors declare no competing interest.

Authors ORCIDs

Tobias J Buscham   http://orcid.org/0000-0002-6916-3102
Maria A Eichel-Vogel   http://orcid.org/0000-0002-9925-7249
Anna M. Steyer   http://orcid.org/0000-0002-4814-7517
Olaf Jahn   http://orcid.org/0000-0002-3397-8924
Nicola Strenzke   http://orcid.org/0000-0003-1673-1046
Rakshit Dadarwal   http://orcid.org/0000-0003-3091-2580
Tor R Memhave   http://orcid.org/0000-0002-3448-1581
Sophie B. Siems   http://orcid.org/0000-0002-7760-2507
Ting Sun   http://orcid.org/0000-0002-7104-7215
Torben Ruhwedel   http://orcid.org/0000-0002-9535-9395
Wiebke Möbius   http://orcid.org/0000-0002-2902-7165
Eva-Maria Krämer Albers http://orcid.org/0000-0001-7994-1185
Susann Boretius   http://orcid.org/0000-0003-2792-7423
Klaus-Armin Nave   http://orcid.org/0000-0001-8724-9666
Hauke B Werner   http://orcid.org/0000-0002-7710-5738

References

Ambrozkiewicz, M. C., Schwark, M., Kishimoto-Suga, M., Borisova, E., Hori, K., Salazar-Lázaro, A., Rusanova, A., Altas, B., Piepkorn, L., Bessa, P., Schaub, T., Zhang, X., Rabe, T., Ripamonti, S., Rosário, M., Akiyama, H., Jahn, O., Kobayashi, T., Hoshino, M., … Kawabe, H. (2018). Polarity Acquisition in Cortical Neurons Is Driven by Synergistic Action of Sox9-Regulated Wwp1 and Wwp2 E3 Ubiquitin Ligases and Intronic miR-140. *Neuron*, *100*(5), 1097-1115.e15. https://doi.org/10.1016/j.neuron.2018.10.008

Basser, P. J., Mattiello, J., & Lebihan, D. (1994). MR Diffusion Tensor Spectroscopy and Imaging. *Biophysical Journal*, *66*, 259–267.

Bosanac, T., Hughes, R. O., Engber, T., Devraj, R., Brearley, A., Danker, K., Young, K., Kopatz, J., Hermann, M., Berthemy, A., Boyce, S., Bentley, J., & Krauss, R. (2021). Pharmacological SARM1 inhibition protects axon structure and function in paclitaxel-induced peripheral neuropathy. *Brain*. https://doi.org/10.1093/brain/awab184/6272578

Burr, M. L., Sparbier, C. E., Chan, Y. C., Williamson, J. C., Woods, K., Beavis, P. A., Lam, E. Y. N., Henderson, M. A., Bell, C. C., Stolzenburg, S., Gilan, O., Bloor, S., Noori, T., Morgens, D. W., Bassik, M. C., Neeson, P. J., Behren, A., Darcy, P. K., Dawson, S. J., … Dawson, M. A. (2017). CMTM6 maintains the expression of PD-L1 and regulates anti-Tumour immunity. *Nature*, *549*(7670), 101–105. https://doi.org/10.1038/nature23643

Chamberlain, K. A., Huang, N., Xie, Y., LiCausi, F., Li, S., Li, Y., & Sheng, Z.-H. (2021). Oligodendrocytes enhance axonal energy metabolism by deacetylation of mitochondrial proteins through transcellular delivery of SIRT2. *Neuron*, *109*(21), 3456–3472. https://doi.org/10.1016/j.neuron.2021.08.011

Cohen, C. C. H., Popovic, M. A., Klooster, J., Weil, M. T., Möbius, W., Nave, K. A., & Kole, M. H. P. (2020). Saltatory Conduction along Myelinated Axons Involves a Periaxonal Nanocircuit. *Cell*, *180*(2), 311–322. https://doi.org/10.1016/j.cell.2019.11.039

Coleman, M. P., Conforti, L., Anne Buckmaster, E., Tarlton, A., Ewing, R. M., Brown, M. C., Lyon, M. F., & Perry, V. H. (1998). An 85-kb tandem triplication in the slow Wallerian degeneration (Wld s) mouse. *Proceedings of the National Academy of Sciences*, *95*, 9985–9990. https://doi.org/10.1073/pnas.95.17.9985

Coleman, M. P., & Höke, A. (2020). Programmed axon degeneration: from mouse to mechanism to medicine. *Nature Reviews Neuroscience*, *21*(4), 183–196. https://doi.org/10.1038/s41583-020-0269-3

de Monasterio-Schrader, P., Jahn, O., Tenzer, S., Wichert, S. P., Patzig, J., & Werner, H. B. (2012). Systematic approaches to central nervous system myelin. *Cellular and Molecular Life Sciences*, *69*(17), 2879–2894. https://doi.org/10.1007/s00018-012-0958-9

de Monasterio-Schrader, P., Patzig, J., Möbius, W., Barrette, B., Wagner, T. L., Kusch, K., Edgar, J. M., Brophy, P. J., & Werner, H. B. (2013). Uncoupling of neuroinflammation from axonal degeneration in mice lacking the myelin protein tetraspanin-2. *GLIA*, *61*, 1832–1847. https://doi.org/10.1002/glia.22561

824 Deerinck, T. J., Bushong, E. A., Thor, A., & Ellisman, M. H. (2010). Ncmir methods for 3D
825   EM: A New protocol for preparation of biological specimens for serial block face
826   scanning electron microscopy. *Microscopy*, 6–8.
827   http://scholar.google.com/scholar?start=320&q=Mark+Ellisman&hl=en&as_sdt=0,5#0

828 di Stefano, M., Nascimento-Ferreira, I., Orsomando, G., Mori, V., Gilley, J., Brown, R.,
829   Janeckova, L., Vargas, M. E., Worrell, L. A., Loreto, A., Tickle, J., Patrick, J., Webster,
830   J. R. M., Marangoni, M., Carpi, F. M., Pucciarelli, S., Rossi, F., Meng, W., Sagasti, A.,
831   … Conforti, L. (2015). A rise in NAD precursor nicotinamide mononucleotide (NMN)
832   after injury promotes axon degeneration. *Cell Death and Differentiation*, *22*(5), 731–742.
833   https://doi.org/10.1038/cdd.2014.164

834 Dieck, S. T., Specht, D., Strenzke, N., Hida, Y., Krishnamoorthy, V., Schmidt, K. F., Inoue,
835   E., Ishizaki, H., Tanaka-Okamoto, M., Miyoshi, J., Hagiwara, A., Brandstatter, J. H.,
836   Löwel, S., Gollisch, T., Ohtsuka, T., & Moser, T. (2012). Deletion of the presynaptic
837   scaffold cast reduces active zone size in rod photoreceptors and impairs visual
838   processing. *Journal of Neuroscience*, *32*(35), 12192–12203.
839   https://doi.org/10.1523/JNEUROSCI.0752-12.2012

840 Distler, U., Kuharev, J., Navarro, P., Levin, Y., Schild, H., & Tenzer, S. (2014). Drift time-
841   specific collision energies enable deep-coverage data-independent acquisition
842   proteomics. *Nature Methods*, *11*(2), 167–170. https://doi.org/10.1038/nmeth.2767

843 Edgar, J. M., McLaughlin, M., Werner, H. B., McCulloch, M. C., Barrie, J. A., Brown, A.,
844   Faichney, A. B., Snaidero, N., Nave, K. A., & Griffiths, I. R. (2009). Early ultrastructural
845   defects of axons and axon-glia junctions in mice lacking expression of Cnp1. *GLIA*,
846   *57*(16), 1815–1824. https://doi.org/10.1002/glia.20893

847 Edgar, J. M., McLaughlin, M., Yool, D., Zhang, S. C., Fowler, J. H., Montague, P., Barrie, J.
848   A., McCulloch, M. C., Duncan, I. D., Garbern, J., Nave, K. A., & Griffiths, I. R. (2004).
849   Oligodendroglial modulation of fast axonal transport in a mouse model of hereditary
850   spastic paraplegia. *Journal of Cell Biology*, *166*(1), 121–131.
851   https://doi.org/10.1083/jcb.200312012

852 Eichel, M. A., Gargareta, V. I., D'Este, E., Fledrich, R., Kungl, T., Buscham, T. J., Lüders, K.
853   A., Miracle, C., Jung, R. B., Distler, U., Kusch, K., Möbius, W., Hülsmann, S., Tenzer,
854   S., Nave, K. A., & Werner, H. B. (2020). CMTM6 expressed on the adaxonal Schwann
855   cell surface restricts axonal diameters in peripheral nerves. *Nature Communications*,
856   *11*(1), 4514. https://doi.org/10.1038/s41467-020-18172-7

857 Erwig, M. S., Hesse, D., Jung, R. B., Uecker, M., Kusch, K., Tenzer, S., Jahn, O., & Werner,
858   H. B. (2019). Myelin: Methods for purification and proteome analysis. *Methods in*
859   *Molecular Biology*, *1936*, 37–63. https://doi.org/10.1007/978-1-4939-9072-6_3

860 Erwig, M. S., Patzig, J., Steyer, A. M., Dibaj, P., Heilmann, M., Heilmann, I., Jung, R. B.,
861   Kusch, K., Möbius, W., Jahn, O., Nave, K.-A., & Werner, H. B. (2019). Anillin facilitates
862   septin assembly to prevent pathological outfoldings of central nervous system myelin.
863   *ELife*, *8*, e43888. https://doi.org/10.7554/eLife.43888.001

864 Fadnavis, S., Batson, J., & Garyfallidis, E. (2020). *Patch2Self: Denoising Diffusion MRI with*
865   *Self-Supervised Learning*. http://arxiv.org/abs/2011.01355

866   Farley, F. W., Soriano, P., Steffen, L. S., & Dymecki, S. M. (2000). Widespread
867   Recombinase Expression Using FLPeR (Flipper) Mice. *Genesis*, *28*, 106–110.

868   Franklin, R. J. M., Ffrench-Constant, C., Edgar, J. M., & Smith, K. J. (2012). Neuroprotection
869   and repair in multiple sclerosis. *Nature Reviews Neurology*, *8*(11), 624–634.
870   https://doi.org/10.1038/nrneurol.2012.200

871   Frühbeis, C., Kuo-Elsner, W. P., Müller, C., Barth, K., Peris, L., Tenzer, S., Möbius, W.,
872   Werner, H. B., Nave, K. A., Fröhlich, D., & Krämer-Albers, E. M. (2020).
873   Oligodendrocytes support axonal transport and maintenance via exosome secretion.
874   *PLoS Biology*, *18*, e3000621. https://doi.org/10.1371/journal.pbio.3000621

875   Fünfschilling, U., Supplie, L. M., Mahad, D., Boretius, S., Saab, A. S., Edgar, J., Brinkmann,
876   B. G., Kassmann, C. M., Tzvetanova, I. D., Möbius, W., Diaz, F., Meijer, D., Suter, U.,
877   Hamprecht, B., Sereda, M. W., Moraes, C. T., Frahm, J., Goebbels, S., & Nave, K. A.
878   (2012). Glycolytic oligodendrocytes maintain myelin and long-term axonal integrity.
879   *Nature*, *485*(7399), 517–521. https://doi.org/10.1038/nature11007

880   Garyfallidis, E., Brett, M., Amirbekian, B., Rokem, A., van der Walt, S., Descoteaux, M., &
881   Nimmo-Smith, I. (2014). Dipy, a library for the analysis of diffusion MRI data. *Frontiers in
882   Neuroinformatics*, *8*(18). https://doi.org/10.3389/fninf.2014.00008

883   Gerdts, J., Summers, D. W., Sasaki, Y., DiAntonio, A., & Milbrandt, J. (2013). Sarm1-
884   mediated axon degeneration requires both SAM and TIR interactions. *Journal of
885   Neuroscience*, *33*(33), 13569–13580. https://doi.org/10.1523/JNEUROSCI.1197-
886   13.2013

887   Ghandour, M. S., Vincendon, G., Gombos, A., Limozin, N., Filippi, D., Dalmasso, C., &
888   Laurent, G. (1980). Carbonic Anhydrase and Oligodendroglia in Developing Rat
889   Cerebellum: A Biochemical and Immunohistological Study. *Developmental Biology*, *77*,
890   73–83.

891   Gilley, J., & Coleman, M. P. (2010). Endogenous Nmnat2 Is an Essential Survival Factor for
892   Maintenance of Healthy Axons. *PLoS Biology*, *8*(1), e1000300.
893   https://doi.org/10.1371/journal.pbio.1000300

894   Gong, S., Doughty, M., Harbaugh, C. R., Cummins, A., Hatten, M. E., Heintz, N., & Gerfen,
895   C. R. (2007). Targeting Cre recombinase to specific neuron populations with bacterial
896   artificial chromosome constructs. *Journal of Neuroscience*, *27*(37), 9817–9823.
897   https://doi.org/10.1523/JNEUROSCI.2707-07.2007

898   Griffiths I, Klugmann M, Anderson T, Thomson C, Vouyiouklis D, & Nave KA. (1998). Axonal
899   swellings and degeneration in mice lacking the major proteolipid of myelin. *Science*,
900   *280*, 1610–1613.

901   Hagemeyer, N., Goebbels, S., Papiol, S., Kästner, A., Hofer, S., Begemann, M., Gerwig, U.
902   C., Boretius, S., Wieser, G. L., Ronnenberg, A., Gurvich, A., Heckers, S. H., Frahm, J.,
903   Nave, K. A., & Ehrenreich, H. (2012). A myelin gene causative of a catatonia-depression
904   syndrome upon aging. *EMBO Molecular Medicine*, *4*(6), 528–539.
905   https://doi.org/10.1002/emmm.201200230

906   Han, W., Ding, P., Xu, M., Wang, L., Rui, M., Shi, S., Liu, Y., Zheng, Y., Chen, Y., Yang, T.,
907   & Ma, D. (2003). Identification of eight genes encoding chemokine-like factor

908 superfamily members 1-8 (CKLFSF1-8) by in silico cloning and experimental validation.
909 *Genomics*, *81*(6), 609–617. https://doi.org/10.1016/S0888-7543(03)00095-8

910 Hartline, D. K., & Colman, D. R. (2007). Rapid Conduction and the Evolution of Giant Axons
911 and Myelinated Fibers. *Current Biology*, *17*(1), 29–35.
912 https://doi.org/10.1016/j.cub.2006.11.042

913 Helms, G., Dathe, H., Kallenberg, K., & Dechent, P. (2008). High-resolution maps of
914 magnetization transfer with inherent correction for RF inhomogeneity and T1 relaxation
915 obtained from 3D FLASH MRI. *Magnetic Resonance in Medicine*, *60*(6), 1396–1407.
916 https://doi.org/10.1002/mrm.21732

917 Hopkins, E. L., Gu, W., Kobe, B., & Coleman, M. P. (2021). A Novel NAD Signaling
918 Mechanism in Axon Degeneration and its Relationship to Innate Immunity. *Frontiers in*
919 *Molecular Biosciences*, *8*, 703532. https://doi.org/10.3389/fmolb.2021.703532

920 Hughes, R. O., Bosanac, T., Mao, X., Engber, T. M., DiAntonio, A., Milbrandt, J., Devraj, R.,
921 & Krauss, R. (2021). Small Molecule SARM1 Inhibitors Recapitulate the SARM1−/−
922 Phenotype and Allow Recovery of a Metastable Pool of Axons Fated to Degenerate.
923 *Cell Reports*, *34*(1), 108588. https://doi.org/10.1016/j.celrep.2020.108588

924 Ishii, A., Dutta, R., Wark, G. M., Hwang, S.-I., Han, D. K., Trapp, B. D., Pfeiffer, S. E., &
925 Bansal, R. (2009). Human myelin proteome and comparative analysis with mouse
926 myelin. *PNAS*, *106*(34), 14605–14610. www.pnas.org/cgi/content/full/

927 Jahn, O., Siems, S. B., Kusch, K., Hesse, D., Jung, R. B., Liepold, T., Uecker, M., Sun, T., &
928 Werner, H. B. (2020). The CNS Myelin Proteome: Deep Profile and Persistence After
929 Post-mortem Delay. *Frontiers in Cellular Neuroscience*, *14*, 239.
930 https://doi.org/10.3389/fncel.2020.00239

931 Jäkel, S., Agirre, E., Mendanha Falcão, A., van Bruggen, D., Lee, K. W., Knuesel, I.,
932 Malhotra, D., ffrench-Constant, C., Williams, A., & Castelo-Branco, G. (2019). Altered
933 human oligodendrocyte heterogeneity in multiple sclerosis. *Nature*, *566*(7745), 543–
934 547. https://doi.org/10.1038/s41586-019-0903-2

935 Jumper, J., Evans, R., Pritzel, A., Green, T., Figurnov, M., Ronneberger, O.,
936 Tunyasuvunakool, K., Bates, R., Žídek, A., Potapenko, A., Bridgland, A., Meyer, C.,
937 Kohl, S. A. A., Ballard, A. J., Cowie, A., Romera-Paredes, B., Nikolov, S., Jain, R.,
938 Adler, J., … Hassabis, D. (2021). Highly accurate protein structure prediction with
939 AlphaFold. *Nature*, *596*(7873), 583–589. https://doi.org/10.1038/s41586-021-03819-2

940 Jung, M., Sommer, I., Schachner, M., & Nave, K.-A. (1996). Monoclonal Antibody O10
941 Defines a Conformationally Sensitive Cell-Surface Epitope of Proteolipid Protein (PLP):
942 Evidence that PLP Misfolding Underlies Dysmyelination in Mutant Mice. *The Journal of*
943 *Neuroscience*, *16*(24), 7920–7929.

944 Kagawa, T., Mekada, E., Shishido, Y., & Ikenaka, K. (1997). Immune System-Related CD9 Is
945 Expressed in Mouse Central Nervous System Myelin at a Very Late Stage of
946 Myelination. *J. Neurosci. Res*, *50*, 312–320.

947 Kleopa, K. A., Orthmann, J. L., Enriquez, A., Paul, D. L., & Scherer, S. S. (2004). Unique
948 distributions of the gap junction proteins connexin29, connexin32, and connexin47 in
949 oligodendrocytes. *GLIA*, *47*(4), 346–357. https://doi.org/10.1002/glia.20043

950   Klugmann, M., & Schwab, M. H. (1997). Assembly of CNS Myelin in the Absence of
951   Proteolipid Protein. *Neuron*, *18*, 59–70.

952   Kuharev, J., Navarro, P., Distler, U., Jahn, O., & Tenzer, S. (2015). In-depth evaluation of
953   software tools for data-independent acquisition based label-free quantification.
954   *Proteomics*, *15*(18), 3140–3151. https://doi.org/10.1002/pmic.201400396

955   Lappe-Siefke, C., Goebbels, S., Gravel, M., Nicksch, E., Lee, J., Braun, P. E., Griffiths, I. R.,
956   & Navel, K. A. (2003). Disruption of Cnp1 uncouples oligodendroglial functions in axonal
957   support and myelination. *Nature Genetics*, *33*(3), 366–374.
958   https://doi.org/10.1038/ng1095

959   Lee, Y., Morrison, B. M., Li, Y., Lengacher, S., Farah, M. H., Hoffman, P. N., Liu, Y.,
960   Tsingalia, A., Jin, L., Zhang, P. W., Pellerin, L., Magistretti, P. J., & Rothstein, J. D.
961   (2012). Oligodendroglia metabolically support axons and contribute to
962   neurodegeneration. *Nature*, *487*(7408), 443–448. https://doi.org/10.1038/nature11314

963   Leone, D. P., Genoud, S., Atanasoski, S., Grausenburger, R., Berger, P., Metzger, D.,
964   Macklin, W. B., Chambon, P., & Suter, U. (2003). Tamoxifen-inducible glia-specific Cre
965   mice for somatic mutagenesis in oligodendrocytes and Schwann cells. *Molecular and
966   Cellular Neuroscience*, *22*(4), 430–440. https://doi.org/10.1016/S1044-7431(03)00029-0

967   Loring, H. S., Parelkar, S. S., Mondal, S., & Thompson, P. R. (2020). Identification of the first
968   noncompetitive SARM1 inhibitors. *Bioorganic and Medicinal Chemistry*, *28*(18), 115644.
969   https://doi.org/10.1016/j.bmc.2020.115644

970   Lüders, K. A., Nessler, S., Kusch, K., Patzig, J., Jung, R. B., Möbius, W., Nave, K. A., &
971   Werner, H. B. (2019). Maintenance of high proteolipid protein level in adult central
972   nervous system myelin is required to preserve the integrity of myelin and axons. *GLIA*,
973   *67*(4), 634–649. https://doi.org/10.1002/glia.23549

974   Lüders, K. A., Patzig, J., Simons, M., Nave, K. A., & Werner, H. B. (2017). Genetic dissection
975   of oligodendroglial and neuronal Plp1 function in a novel mouse model of spastic
976   paraplegia type 2. *GLIA*, *65*(11), 1762–1776. https://doi.org/10.1002/glia.23193

977   Lunn, E. R., Perry, V. H., Brown, M. C., & Gordon', S. (1989). Absence of Wallerian
978   Degeneration does not Hinder Regeneration in Peripheral Nerve. *European Journal of
979   Neuroscience*, *I*(1), 27–33.

980   Mack, T. G. A., Reiner, M., Beirowski, B., Mi, W., Emanuelli, M., Wagner, D., Thomson, D.,
981   Gillingwater, T., Court, F., Conforti, L., Fernando, F. S., Tarlton, A., Andressen, C.,
982   Addicks, K., Magni, G., Ribchester, R. R., Perry, V. H., & Coleman, M. P. (2001).
983   Wallerian degeneration of injured axons and synapses is delayed by a Ube4b/Nmnat
984   chimeric gene. *Nature Neuroscience*, *4*(12), 1199–1206. https://doi.org/10.1038/nn770

985   Mezzadra, R., Sun, C., Jae, L. T., Gomez-Eerland, R., de Vries, E., Wu, W., Logtenberg, M.
986   E. W., Slagter, M., Rozeman, E. A., Hofland, I., Broeks, A., Horlings, H. M., Wessels, L.
987   F. A., Blank, C. U., Xiao, Y., Heck, A. J. R., Borst, J., Brummelkamp, T. R., &
988   Schumacher, T. N. M. (2017). Identification of CMTM6 and CMTM4 as PD-L1 protein
989   regulators. *Nature*, *549*(7670), 106–110. https://doi.org/10.1038/nature23669

990   Möbius, W., Cooper, B., Kaufmann, W. A., Imig, C., Ruhwedel, T., Snaidero, N., Saab, A. S.,
991   & Varoqueaux, F. (2010). Electron microscopy of the mouse central nervous system.

27

Methods in Cell Biology, *96*(C), 475–512. https://doi.org/10.1016/S0091-679X(10)96020-2

Mukherjee, C., Kling, T., Russo, B., Miebach, K., Kess, E., Schifferer, M., Pedro, L. D., Weikert, U., Fard, M. K., Kannaiyan, N., Rossner, M., Aicher, M. L., Goebbels, S., Nave, K. A., Krämer-Albers, E. M., Schneider, A., & Simons, M. (2020). Oligodendrocytes Provide Antioxidant Defense Function for Neurons by Secreting Ferritin Heavy Chain. *Cell Metabolism*, *32*(2), 259-272.e10. https://doi.org/10.1016/j.cmet.2020.05.019

Osterloh, J. M., Yang, J., Rooney, T. M., Fox, A. N., Adalbert, R., Powell, E. H., Sheehan, A. E., Avery, M. A., Hackett, R., Logan, M. A., MacDonald, J. M., Ziegenfuss, J. S., Milde, S., Hou, Y. J., Nathan, C., Ding, A., Brown, R. H., Conforti, L., Coleman, M., … Freeman, M. R. (2012). dSarm/Sarm1 is required for activation of an injury-induced axon death pathway. *Science*, *337*(6093), 481–484. https://doi.org/10.1126/science.1223899

Ou, X., Sun, S. W., Liang, H. F., Song, S. K., & Gochberg, D. F. (2009). Quantitative magnetization transfer measured pool-size ratio reflects optic nerve myelin content in Ex vivo mice. *Magnetic Resonance in Medicine*, *61*(2), 364–371. https://doi.org/10.1002/mrm.21850

Patzig, J., Erwig, M. S., Tenzer, S., Kusch, K., Dibaj, P., Möbius, W., Goebbels, S., Schaeren-Wiemers, N., Nave, K. A., & Werner, H. B. (2016). Septin/anillin filaments scaffold central nervous system myelin to accelerate nerve conduction. *ELife*, *5*, e17119. https://doi.org/10.7554/eLife.17119.001

Pei, M., Nguyen, T. D., Thimmappa, N. D., Salustri, C., Dong, F., Cooper, M. A., Li, J., Prince, M. R., & Wang, Y. (2015). Algorithm for fast monoexponential fitting based on Auto-Regression on Linear Operations (ARLO) of data. *Magnetic Resonance in Medicine*, *73*(2), 843–850. https://doi.org/10.1002/mrm.25137

Perez-Riverol, Y., Csordas, A., Bai, J., Bernal-Llinares, M., Hewapathirana, S., Kundu, D. J., Inuganti, A., Griss, J., Mayer, G., Eisenacher, M., Pérez, E., Uszkoreit, J., Pfeuffer, J., Sachsenberg, T., Yilmaz, Ş., Tiwary, S., Cox, J., Audain, E., Walzer, M., … Vizcaíno, J. A. (2019). The PRIDE database and related tools and resources in 2019: Improving support for quantification data. *Nucleic Acids Research*, *47*(D1), D442–D450. https://doi.org/10.1093/nar/gky1106

Philips, T., Mironova, Y. A., Jouroukhin, Y., Chew, J., Vidensky, S., Farah, M. H., Pletnikov, M. v., Bergles, D. E., Morrison, B. M., & Rothstein, J. D. (2021). MCT1 Deletion in Oligodendrocyte Lineage Cells Causes Late-Onset Hypomyelination and Axonal Degeneration. *Cell Reports*, *34*(2), 108610. https://doi.org/10.1016/j.celrep.2020.108610

Provencher, S. W. (1993). Estimation of Metabolite Concentrations from Localized in Vivo Proton NMR Spectra. In *Magnetic Resonance in Medicine* (Vol. 30, pp. 672–679).

Rasband, M. N., Tayler, J., Kaga, Y., Yang, Y., Lappe-Siefke, C., Nave, K. A., & Bansal, R. (2005). CNP is required for maintenance of axon-glia interactions at nodes of ranvier in the CNS. *GLIA*, *50*(1), 86–90. https://doi.org/10.1002/glia.20165

Ridder, W. H., & Nusinowitz, S. (2006). The visual evoked potential in the mouse - Origins and response characteristics. *Vision Research*, *46*(6–7), 902–913. https://doi.org/10.1016/j.visres.2005.09.006

1035 Roach, A., Takahashi, N., Pravtcheva, D., Ruddle, F., & Hood, L. (1985). Chromosomal
1036   Mapping of Mouse Myelin Basic Protein Gene and Structure and Transcription of the
1037   Partially Deleted Gene in Shiverer Mutant Mice. *Cell*, *42*, 149–155.

1038 Saab, A. S., Tzvetavona, I. D., Trevisiol, A., Baltan, S., Dibaj, P., Kusch, K., Möbius, W.,
1039   Goetze, B., Jahn, H. M., Huang, W., Steffens, H., Schomburg, E. D., Pérez-Samartín,
1040   A., Pérez-Cerdá, F., Bakhtiari, D., Matute, C., Löwel, S., Griesinger, C., Hirrlinger, J., …
1041   Nave, K. A. (2016). Oligodendroglial NMDA Receptors Regulate Glucose Import and
1042   Axonal Energy Metabolism. *Neuron*, *91*(1), 119–132.
1043   https://doi.org/10.1016/j.neuron.2016.05.016

1044 Samsam, M., Mi, W., Wessig, C., Zielasek, J., Toyka, K. v, Coleman, M. P., & Martini, R.
1045   (2003). The Wlds Mutation Delays Robust Loss of Motor and Sensory Axons in a
1046   Genetic Model for Myelin-Related Axonopathy. *The Journal of Neuroscience*, *23*(7),
1047   2833–2839.

1048 Schardt, A., Brinkmann, B. G., Mitkovski, M., Sereda, M. W., Werner, H. B., & Nave, K. A.
1049   (2009). The SNARE protein SNAP-29 interacts with the GTPase Rab3A: Implications for
1050   membrane trafficking in myelinating glia. *Journal of Neuroscience Research*, *87*(15),
1051   3465–3479. https://doi.org/10.1002/jnr.22005

1052 Schindelin, J., Arganda-Carreras, I., Frise, E., Kaynig, V., Longair, M., Pietzsch, T.,
1053   Preibisch, S., Rueden, C., Saalfeld, S., Schmid, B., Tinevez, J. Y., White, D. J.,
1054   Hartenstein, V., Eliceiri, K., Tomancak, P., & Cardona, A. (2012). Fiji: An open-source
1055   platform for biological-image analysis. *Nature Methods*, *9*(7), 676–682.
1056   https://doi.org/10.1038/nmeth.2019

1057 Shao, L., Cui, Y., Li, H., Liu, Y., Zhao, H., Wang, Y., Zhang, Y., Ka, M. N., Han, W., Ma, D., &
1058   Tao, Q. (2007). CMTM5 exhibits tumor suppressor activities and is frequently silenced
1059   by methylation in carcinoma cell lines. *Clinical Cancer Research*, *13*(19), 5756–5762.
1060   https://doi.org/10.1158/1078-0432.CCR-06-3082

1061 Siems, S. B., Jahn, O., Eichel, M. A., Kannaiyan, N., Wu, L. M. N., Sherman, D. L., Kusch,
1062   K., Hesse, D., Jung, R. B., Fledrich, R., Sereda, M. W., Rossner, M. J., Brophy, P. J., &
1063   Werner, H. B. (2020). Proteome profile of peripheral myelin in healthy mice and in a
1064   neuropathy model. *ELife*, *9*, e51406. https://doi.org/10.7554/eLife.51406

1065 Silva, J. C., Gorenstein, M. v., Li, G. Z., Vissers, J. P. C., & Geromanos, S. J. (2006).
1066   Absolute quantification of proteins by LCMSE: A virtue of parallel MS acquisition.
1067   *Molecular and Cellular Proteomics*, *5*(1), 144–156.
1068   https://doi.org/10.1074/mcp.M500230-MCP200

1069 Stadelmann, C., Timmler, S., Barrantes-Freer, A., & Simons, M. (2019). Myelin in the Central
1070   Nervous System: Structure, Function, and Pathology. *Physiol Rev*, *99*, 1381–1431.
1071   https://doi.org/10.1152/physrev.00031.2018.-Oligodendro

1072 Steyer, A. M., Ruhwedel, T., Nardis, C., Werner, H. B., Nave, K. A., & Möbius, W. (2020).
1073   Pathology of myelinated axons in the PLP-deficient mouse model of spastic paraplegia
1074   type 2 revealed by volume imaging using focused ion beam-scanning electron
1075   microscopy. *Journal of Structural Biology*, *210*(2), 107492.
1076   https://doi.org/10.1016/j.jsb.2020.107492

1077   Tasaki, I. (1939). The electro-saltatory transmission of the nerve impulse and the effect of
1078   narcosis upon the nerve fiber. *The American Journal of Physiology*, *127*(2), 211–227.
1079   https://doi.org/10.1152/AJPLEGACY.1939.127.2.211

1080   Trevisiol, A., Kusch, K., Steyer, A. M., Gregor, I., Nardis, C., Winkler, U., Köhler, S.,
1081   Restrepo, A., Möbius, W., Werner, H. B., Nave, K. A., & Hirrlinger, J. (2020). Structural
1082   myelin defects are associated with low axonal ATP levels but rapid recovery from
1083   energy deprivation in a mouse model of spastic paraplegia. *PLoS Biology*, *18*(11),
1084   e3000943. https://doi.org/10.1371/journal.pbio.3000943

1085   Uschkureit, T., Spörkel, O., Stracke, J., Bü, H., & Stoffel, W. (2000). Early Onset of Axonal
1086   Degeneration in Double (plp/mag/) and Hypomyelinosis in Triple (plp/mbp/mag/) Mutant
1087   Mice. *The Journal of Neuroscience*, *20*(14), 5225–5233.

1088   Wang, J., Zhai, Q., Chen, Y., Lin, E., Gu, W., McBurney, M. W., & He, Z. (2005). A local
1089   mechanism mediates NAD-dependent protection of axon degeneration. *Journal of Cell
1090   Biology*, *170*(3), 349–355. https://doi.org/10.1083/jcb.200504028

1091   Weil, M. T., Heibeck, S., Töpperwien, M., Tom Dieck, S., Ruhwedel, T., Salditt, T., Rodicio,
1092   M. C., Morgan, J. R., Nave, K. A., Möbius, W., & Werner, H. B. (2018). Axonal
1093   ensheathment in the nervous system of lamprey: Implications for the evolution of
1094   myelinating glia. *Journal of Neuroscience*, *38*(29), 6586–6596.
1095   https://doi.org/10.1523/JNEUROSCI.1034-18.2018

1096   Werner, H. B., Krämer-Albers, E. M., Strenzke, N., Saher, G., Tenzer, S., Ohno-Iwashita, Y.,
1097   de Monasterio-Schrader, P., Möbius, W., Moser, T., Griffiths, I. R., & Nave, K. A. (2013).
1098   A critical role for the cholesterol-associated proteolipids PLP and M6B in myelination of
1099   the central nervous system. *GLIA*, *61*(4), 567–586. https://doi.org/10.1002/glia.22456

1100   Wieser, G. L., Gerwig, U. C., Adamcio, B., Barrette, B., Nave, K. A., Ehrenreich, H., &
1101   Goebbels, S. (2013). Neuroinflammation in white matter tracts of Cnp1 mutant mice
1102   amplified by a minor brain injury. *GLIA*, *61*(6), 869–880.
1103   https://doi.org/10.1002/glia.22480

1104   Wolf, N. I., ffrench-Constant, C., & van der Knaap, M. S. (2021). Hypomyelinating
1105   leukodystrophies — unravelling myelin biology. *Nature Reviews Neurology*, *17*(2), 88–
1106   103. https://doi.org/10.1038/s41582-020-00432-1

1107   Xiao, Y., Yuan, Y., Zhang, Y., Li, J., Liu, Z., Zhang, X., Sheng, Z., Xu, T., & Wang, X. (2015).
1108   CMTM5 is reduced in prostate cancer and inhibits cancer cell growth in vitro and in vivo.
1109   *Clinical and Translational Oncology*, *17*(6), 431–437. https://doi.org/10.1007/s12094-
1110   014-1253-z

1111   Yuan, Y., Sheng, Z., Liu, Z., Zhang, X., Xiao, Y., Xie, J., Zhang, Y., & Xu, T. (2020). CMTM5-
1112   v1 inhibits cell proliferation and migration by downregulating oncogenic EGFR signaling
1113   in prostate cancer cells. *Journal of Cancer*, *11*(13), 3762–3770.
1114   https://doi.org/10.7150/jca.42314

1115   Zhang, Y., Chen, K., Sloan, S. A., Bennett, M. L., Scholze, A. R., O'Keeffe, S., Phatnani, H.
1116   P., Guarnieri, P., Caneda, C., Ruderisch, N., Deng, S., Liddelow, S. A., Zhang, C.,
1117   Daneman, R., Maniatis, T., Barres, B. A., & Wu, J. Q. (2014). An RNA-sequencing
1118   transcriptome and splicing database of glia, neurons, and vascular cells of the cerebral

1119   cortex. *Journal of Neuroscience*, *34*(36), 11929–11947.
1120   https://doi.org/10.1523/JNEUROSCI.1860-14.2014

1121 Zhou, Y., Song, W. M., Andhey, P. S., Swain, A., Levy, T., Miller, K. R., Poliani, P. L.,
1122   Cominelli, M., Grover, S., Gilfillan, S., Cella, M., Ulland, T. K., Zaitsev, K., Miyashita, A.,
1123   Ikeuchi, T., Sainouchi, M., Kakita, A., Bennett, D. A., Schneider, J. A., … Colonna, M.
1124   (2020). Human and mouse single-nucleus transcriptomics reveal TREM2-dependent
1125   and TREM2-independent cellular responses in Alzheimer's disease. *Nature Medicine*,
1126   *26*(1), 131–142. https://doi.org/10.1038/s41591-019-0695-9

1127
1128

1129 **Figure legends**

1130

1131 **Figure 1: Identification of CMTM5 as a CNS myelin protein.**

1132 **(A)** Immunoblot analysis of CMTM5 in myelin biochemically purified from the brains C57/Bl6

1133 mice at the age of 75 days compared to brain lysate with the same amount of protein loaded

1134 onto the gel. Note that CMTM5 is enriched in myelin. Known myelin proteins PLP, CNP and

1135 SIRT2 are detected as markers. Shown are three biological replicates.

1136 **(B)** Immunohistochemistry and confocal microscopy of spinal cord sections of mice at the age

1137 of 75 days. Note that CMTM5 (magenta) labelling was consistent with localization in myelin

1138 surrounding beta-III tubulin (TUJ1)-immunopositive axons (yellow) in CTRL (*Cmtm5$^{fl/fl}$*) mice.

1139 CMTM5 labelling was not detected in myelin of mice lacking *Cmtm5* expression in mature

1140 oligodendrocytes (*Cmtm5$^{fl/fl}$*Cnp$^{Cre/Wt}$*, cKO). Scale bar, 2 μm.

1141 **(C, D)** Immunoblot analysis of CMTM5 in brain lysate **(C)** and biochemically purified myelin **(D)**

1142 of young and aged mice. Note that CMTM5 abundance in brain lysate increases coinciding

1143 with developmental myelination **(D)**. Shown is one biological replicate per age. PLP, CNP,

1144 SIRT2 were detected as markers. P= postnatal day, m=months.

1145

1146

1147 **Figure 1-Supplement 1: *Cmtm5* mRNA is expressed in mature oligodendrocytes of mice**

1148 **and humans.**

1149 **(A, B)** Abundance of *Cmtm5* mRNA according to bulk RNAseq data of cells immunopanned

1150 from mouse cortices (Zhang et al., 2014). Note that among all members of the CMTM family,

1151 only *Cmtm5* mRNA is considerably expressed in MOL **(A)**. Increasing *Cmtm5* mRNA

1152 expression coincides with maturation of cells of the oligodendrocyte lineage **(B)**. OPC,

1153 oligodendrocyte precursor cells; NFO, newly formed oligodendrocyte; MOL, Mature

1154 oligodendrocytes; FPKM, fragments per kilobase per million mapped fragments. Data

1155 represented as mean ± SEM.

1156 **(C, D)** Uniform manifold approximation and projection (UMAP) feature plots of scRNAseq data

1157 derived from a previously published dataset (Zhou et al., 2020) shows enriched expression of

1158 *Cmtm5* mRNA in mature oligodendrocytes (MOL) of mice **(C)**. *Mbp* serves as a marker gene

1159 for MOL in mice **(D)**.

1160 **(E, F)** UMAP feature plots of scRNAseq data derived from a previously published dataset

1161 (Jäkel et al., 2019) shows enriched expression of *CMTM5* mRNA in mature oligodendrocytes

1162 (MOL) of the white matter in disease-unaffected human control samples **(E)**. *MBP* serves a

1163 marker gene for human MOL **(F)**.

1164

1165

32

1166   **Figure 2: CMTM5 is not essential for myelin biogenesis and composition.**

1167   **(A)** Immunoblot analysis shows that CMTM5 is undetectable in myelin purified from the brains

1168   of *Cmtm5^fl/fl*Cnp^Cre/Wt* (cKO) mice. PLP, CNP, SIRT2 were detected as markers. Shown are

1169   three biological replicates per genotype.

1170   **(B,B')** Quantitative proteome analysis of brain myelin reveals largely similar myelin

1171   composition in *Cmtm5* cKO and CTRL mice. Analyzed were n=3 mice per genotype and 2

1172   technical replicates per mouse (see **Figure 2B source data 1**). **(B)** Volcano plot with data

1173   points representing log2-fold change and -log10-transformed q-values of 428 identified

1174   proteins in cKO compared to CTRL myelin. Red dots highlight known myelin proteins. Stippled

1175   lines indicate thresholds. CMTM5 is not displayed because it was not identified in *Cmtm5* cKO

1176   myelin. **(B')** Heatmap showing the relative abundance of selected known myelin proteins in

1177   *Cmtm5* cKO compared to control myelin. Data represents n=3 mice per genotype analyzed as

1178   2 technical replicates per mouse (T1-T6). Note that the relative abundance of most myelin

1179   proteins was essentially similar in cKO and CTRL myelin. In agreement with the immunoblot

1180   analysis in **(A)** the abundance of CNP was about halved in *Cmtm5* cKO myelin reflecting that

1181   the Cre driver line (*Cnp^Cre/Wt*) possesses only one *Cnp* allele. CMTM5 was not detected (n.d.)

1182   in cKO myelin.

1183   **(C-L)** Electron micrographs and quantitative assessment of myelin in CTRL and cKO optic

1184   nerves at postnatal day 30 (P30) **(C-G)** and P75 **(H-L)**. Scale bar, 1µm. Percentage of

1185   unmyelinated axons **(D, I)** and pathological myelin profiles is similar between the groups **(E,**

1186   **J)**. Data correspond to all axons (on average more than 1500 axons) from 18-20 non-

1187   overlapping random EM images from 4-5 animals per group. Two-tailed Student´s t-test, **D**: p=

1188   0.1003; **E**: p= 0.0598; **I**: p= 0.3937; **J**: p= 0.7269. Mean g-ratio **(F, K)** is similar between the

1189   experimental groups at P30 and P75. Data corresponds to 180-200 axons randomly selected

1190   from 18-20 EM images for each mouse. n= 4-5 mice per group. Two-tailed Student´s t-test **F**:

1191   p= 0.5839; **K**: p= 0.8821. **(G, L)** Scatter plot showing g-ratios in relation to respective axonal

1192   diameters. No apparent shift between the experimental groups is detectable.

1193   **(M, N)** Immunohistochemistry and genotype-dependent quantification of CAII immune-positive

1194   oligodendrocytes in a representative white matter tract (hippocampal fimbria) at P75. **(M)**

1195   Representative fluorescence micrograph, stippled lines encircle CAII positive cells. Scale bar,

1196   20 µm. **(N)** Number of CAII immunopositive cells number is similar in the fimbria of CTRL and

1197   *Cmtm5* cKO mice. n= 5-6 mice per group, unpaired Student´s t-test p= 0.5971. Bar graphs

1198   give mean ± SEM; Data points in bar graphs represent induvial mice.

1199

1200

1201   **Figure 2-Supplement 1: MRI of the brains of *Cmtm5* cKO mice.**

33

(A) Magnetic resonance imaging (MRI)-based morphometry of brains from CTRL and *Cmtm5* cKO mice at 8 months of age. Shown are representative genotype averaged (4 mice per genotype) effective transverse relaxation rate (R_2^*) MRI images.

(B-E) Diffusion tensor imaging (DTI) indicates unchanged fractional anisotropy (FA), mean diffusivity (MD), axial diffusivity (AD) and radial diffusivity (RD) in white and grey matter in brains of *Cmtm5* cKO and CTRL mice. CC, Corpus callosum; Fim, Fimbria; Thal, Thalamus; Cort, Cortex; AC, Anterior commissure. n=4 per genotype. Precise p-values are given in the statistics section.

(F) Magnetization transfer saturation index (MTsaT) is unaltered in *Cmtm5* cKO compared to CTRL mice. Exact p-values are listed in the statistics section. All graphs give mean ± SEM; all data points represent individual mice.

Figure 2B source data 1. Label-free quantification of proteins in CNS myelin fractions from Cmtm5 cKO and control mice

Identification and quantification data of proteins detected in myelin by DRE-UDMSe. For each of the two conditions, tryptic peptides derived from two technical replicates (replicate digestion) per each of three biological replicates were analyzed by LC-MS (12 runs in total). Proteins (FDR < 1%; 2 peptides/protein) and peptides (FDR < 1%; ≥6 amino acids) were identified by database search against the UniprotKB/SwissProt mouse database using PLGS. Data were post-processed with the software package ISOQuant to calculate absolute in-sample amounts for each detected protein based on the TOP3 approach. Reported abundance values are defined as the relative amount of each protein in respect to the sum over all detected proteins (ppm: parts per million (w/w) of total protein). Typical contaminant proteins like albumin, hemoglobins, and keratins were filtered. The -log10-transformed q-value (column minuslog10q.mod) was plotted against the log2-transformed fold change (column logFC Cmtm5 cKO/CTRL) to obtain the volcano plot shown in Figure 2B. As no imputation of missing values was performed, proteins exclusive for only one of the conditions do not appear in the volcano plot, but are appended at the end of the list. Criteria for statistically significant regulation were as follows: fold change of at least 2.0 (logFC cKO/CTRL > 1) and q-value below 0.01 (minuslog10q.mod > 2.0). Proteins are sorted in descending order for zdist (see column descriptions below).

Figure 3: *Cmtm5* deletion in oligodendrocytes causes axonopathy.

(A-B) Electron micrographs and genotype-dependent quantitative assessment of CTRL and *Cmtm5* cKO optic nerves at P75. Scale bar, 1μm. **(A)** Arrowheads point at pathological axons.

1239 **(B)** Quantification of pathological profiles reveals progressive axonopathy in optic nerves of

1240 *Cmtm5* cKO mice. n=4-5 mice per group, 18-20 random non-overlapping EM images analyzed,

1241 Two-tailed Student´s t-test P30 p= 0.0011; P75 p= 0.0191 with Welch´s correction; P365

1242 p<0.0001.

1243 **(C)** Quantitative assessment of axonal numbers on semithin optic nerve sections. n=4-5 mice

1244 per group, data represents mean axon number in five 55 µm^2 rectangles per mouse randomly

1245 distributed over the entire optic nerve. Axon numbers are significantly reduced at one year of

1246 age according to Two-tailed Student´s t-test P30 p= 0.1288; P75 p= 0.5993; P365 p=0.0499.

1247 **(D-E)** Electron micrographs and genotype-dependent quantitative assessment of spinal cord

1248 white matter in 1 year old CTRL and *Cmtm5* cKO mice. Scale bar= 1µm. **(F)** Number of

1249 pathological profiles is increased in spinal cord white matter of *Cmtm5* cKO mice. n=3-7 mice

1250 per group, 20 non-overlapping random EM images per mouse, Two-tailed Student´s t-test

1251 p=0.0007. All bars show mean ± SEM; all data points represent individual mice.

1252

1253

1254 **Figure 3-Supplement 1: *Cmtm5* deletion in oligodendrocytes does not affect the calibers**

1255 **of healthy-appearing axons**

1256 **(A-C)** Quantitative assessment of mean axonal diameters in the optic nerves of *Cmtm5* cKO

1257 mice, *Cmtm5*$^{-/-}$ mice and respective controls. Mean axonal diameters are similar between

1258 CTRL and cKO mice at ages P75 **(A)** and P365 **(B)** as well as between *Cmtm5*$^{-/-}$ and control

1259 mice at age P75 **(C)**. Two-sided Student´s t-test. **A**; p=0.7514, **B**; p= 0.5315, **C**; p= 0.8496.

1260 700-800 optic nerve axons on 18-20 electron micrographs were analyzed per mouse in 4-5

1261 mice per genotype and age. All bars show mean ± SEM; all data points represent individual

1262 mice. **(A´-C´)** Frequency distributions of pooled axonal diameters in optic nerves of *Cmtm5*

1263 cKO mice, *Cmtm5*$^{-/-}$ mice and respective controls. No apparent shift in axonal diameters was

1264 detected between CTRL and cKO mice at ages P75 **(A´)** and P365 **(B´)** as well as between

1265 *Cmtm5*$^{-/-}$ and control mice at age P75 **(C´)**. Axonal diameters are the same as used for analysis

1266 of mean axonal diameters in **A-C** but represent pools per genotype and timepoint.

1267

1268

1269 **Figure 3-Supplement 2: MRS of the corpus callosum of *Cmtm5* cKO mice**

1270 **(A, B)** Spectroscopy of key metabolic markers myo-inositol (for microglia and astrocytes, in **A**)

1271 and N-acetyl-aspartate (NAA, for axon/neurons, in **B**). **(A)** The concentration of inositol is

1272 significantly increased in the corpus callosum of *Cmtm5* cKO mice compared to controls. Two-

1273 tailed Student´s t-test of the mean p= 0.0004. **(B)** NAA levels are unchanged in the corpus

1274 callosum of *Cmtm5* cKO mice compared to controls. Two-tailed Student´s t-test of the mean

1275 p= 0.057. All bar graphs give mean ± SEM; all data points represent individual mice.

1276

1277

1278 **Figure 3-Supplement 3: Secondary neuropathology following *Cmtm5* deletion.**

1279 Quantitative assessment of immunohistochemistry detecting neuropathological markers in a

1280 representative white matter tract (hippocampal fimbria) using markers for axonal swellings

1281 (APP), microglia (MAC3, IBA1) and astroglia (GFAP) at ages P30 **(A-D)**, P75 **(E-H)** and 1 year

1282 **(I-L)**. Given is the number of APP-immunopositive axonal swellings **(A, E, I)** the relative area

1283 of immunopositivity for MAC3 **(B, F, J)**, IBA1 **(C, G, K)** and GFAP **(D, H, L)**. Note that *Cmtm5*

1284 cKO fimbriae display a significant increase of all assessed neuropathological markers at one

1285 year of age. n=3-6 mice per group, Two-tailed Student´s t-test **A**: p= 0.3225; **B**: p= 0.7901; **C**:

1286 p= 0.9480; **D**; p=0.9152; **E**: p=0.4413; **F**: With Welch´s correction p= 0.0525; **G**: With Welch´s

1287 correction p= 0.9049; **H**: p=0.6270; **I**: p= 0.0055; **J**: With Welch´s correction p=0.0251; **K**: With

1288 Welch´s correction p<0.0001; **L**: p<0.0001. Bar graphs give mean ± SEM.

1289

1290

1291 **Figure 4: FIB-SEM analysis specifies pathological profiles in *Cmtm5* cKO mice.**

1292 Focused ion beam-scanning electron microscopy (FIB-SEM) micrographs **(A-D)** and 3-

1293 dimensional (3D) reconstruction **(A'-D')** of pathological profiles in *Cmtm5* cKO optic nerve at 1

1294 year of age. **A-C** Scale bar = 1µm. **D** Scale bar = 500 nm. Myelin (cyan), axons (gold), inclusion

1295 (purple) and myelin whorls (blue) are highlighted. Pathological profiles include myelin

1296 outfoldings, inclusions in the inner tongue, inclusions completely engulfed by axoplasm, and

1297 myelin whorls. Analysis of the entire 3D volumes reveals that the relative number of myelin

1298 whorls is significantly increased in cKO mice. FIB-SEM stacks of optic nerves of three mice

1299 per genotype were analyzed. Normalized volume = 10000µm^3. Two-tailed Student´s t-test **A´´**:

1300 p= 0.1882; **B´´**: p= 0.2190; **C´´**: p= 0.2111; **D´´**: p=0.0017. Scale bars 1 µm in **A-C**, 500nm in

1301 **D**. Bar graphs give mean ± SEM.

1302

1303

1304 **Figure 5: Electroretinography and visual evoked potentials of *Cmtm5* cKO mice**

1305 **(A-D)** Electroretinograms (ERG). **(A)** ERG waveforms in response to light flashes at 0.25 cd-

1306 s/m^2 from 11 *Cmtm5* cKO (grand average turquoise, SEM shaded) and 10 CTRL mice (grand

1307 average grey, SEM shaded). **(B)** ERG thresholds are similar between CTRL and *Cmtm5* cKO.

1308 Unpaired Student´s t-test of the mean ±SEM p= 0.13 **(C,D)** Amplitudes of the ERG A and B

1309 waves in response to light flashes of varying intensities in *Cmtm5* cKO (n=11, turquoise) and

1310 CTRL mice (n=11, grey; mean ± SEM) are similar between genotypes. 2-way ANOVA **(C)** p=

1311 0.42, **(D)** p= 0.79.

1312 **(E-H)** Visual evoked potentials (VEP). **(E)** VEP in response to light flashes at 0.01 cd-s/m^2 from
1313 10 *Cmtm5* cKO (grand average turquoise, SEM shaded) and 9 CTRL mice (grand average
1314 grey, SEM shaded) display comparable waveforms dominated by a broad negative wave in
1315 both genotypes. **(F)** VEP thresholds are not significantly different between CTRL and *Cmtm5*
1316 cKO. Unpaired Student´s t-test of the mean ±SEM with Welch´s correction p= 0.33 **(G-H)** VEP
1317 latencies and amplitudes in response to light flashes of varying intensities in *Cmtm5* cKO
1318 (n=10, turquoise) and CTRL mice (n=8, grey; means ± SEM). Note that *Cmtm5* cKO and CTRL
1319 mice show similar VEP latencies but *Cmtm5* cKO mice display reduced VEP amplitudes
1320 compared to CTRL mice. 2-way ANOVA **(G)** p= 0.61 **(H)** p= 0.005.

1321

1322

1323 **Figure 6: Axonopathy in constitutive and tamoxifen-induced *Cmtm5* mutants.**
1324 **(A-C)** Analysis of mice lacking *Cmtm5* expression from all cells (*Cmtm5*$^{-/-}$ mice) and respective
1325 controls. **(A)** Immunoblot confirms absence of CMTM5 in myelin purified from the brains of
1326 *Cmtm5*$^{-/-}$ mice. CNP and SIRT2 were detected as controls. **(B)** Representative electron
1327 micrographs of *Cmtm5*$^{-/-}$ and respective control optic nerves. Arrowhead points at pathological
1328 profile. Scale bar, 1µm. **(C)** Quantitative assessment of 18-20 random non-overlapping EM
1329 micrographs from 4-6 mice per group. Note the progressive increase in pathological appearing
1330 axons in optic nerves of *Cmtm5*$^{-/-}$ mice. P75: p= 0.0406 by Two-sided Student´s t-test with
1331 Welch´s Correction; P365: p< 0.0001 two-sided Student´s t-test.
1332 **(D-F)** Analysis of mice lacking *Cmtm5* expression in mature oligodendrocytes upon induction
1333 by tamoxifen (*Cmtm5*$^{fl/fl}$*Plp^{CreERT2}, iKO) and respective tamoxifen-injected *Cre*^{ERT2}-negative
1334 controls (*Cmtm5*$^{fl/fl}$, CTRL). **(D)** Immunoblot of myelin purified from the brains of mice 4 months
1335 post Tamoxifen injection (PTI). Note that the abundance of CMTM5 is strongly reduced in
1336 *Cmtm5* iKO myelin. PLP and SIRT2 were detected as controls. **(E)** Representative electron
1337 micrographs of *Cmtm5* iKO and CTRL optic nerves. Arrowhead points at pathological profile.
1338 Scale bar, 1µm. **(F)** Quantification of pathological profiles (20 non-overlapping random images
1339 per mouse, n=5 mice per genotype). Number of pathological profiles is significantly increased
1340 4 months PTI (p=0.0282 by Two-sided Student´s t-test with Welch´s correction). Bar graphs
1341 give mean ± SEM; data points represent individual mice.

1342

1343

1344 **Figure 6-Supplement 1: Absence of evidence that the abundance of CMTM5 is altered**
1345 **in CNS myelin of *Plp* or *Cnp* deficient mice.**
1346 **(A, B)** Immunoblot analysis of myelin purified from the brains of *Cnp*$^{-/-}$ **(A)** and *Plp*$^{-/Y}$ **(B)** mice
1347 and respective controls at P75. Note that the relative abundance of CMTM5 in myelin appears
1348 similar. Blots show n=2 mice per genotype. Carbonic anhydrase 2 (CAII) served as control.

1349

1350

1351 **Figure 7: Axonopathy upon *Cmtm5* deletion counteracted by the *Wld^s* mutation.**

1352 **(A)** Retinae dissected from *Cmtm5* cKO and CTRL mice were immunolabelled with antibodies

1353 detecting RBPMS as a marker for Retinal ganglion cells (RGC)**.** Image representative of n=3

1354 retinae. Scale bar= 500 µm. **(B)** Magnification of the inner, middle and outer part of the retina.

1355 **(C)** Quantitative assessment indicates that the number of RGCs is similar between *Cmtm5*

1356 cKO and CTRL mice. Retinae of 1 year old mice were analyzed. Data represent the mean of

1357 3 non-overlapping areas assessed for each zone (inner, middle outer retina), as indicated by

1358 the white boxes in **(A)**. Unpaired Two-sided Student´s t-test inner part: p= 0.8484; middle part:

1359 p= 0.5211; outer part: p= 0.2912.

1360 **(D-E)** Electron micrographs and genotype-dependent quantification of pathological profiles in

1361 the optic nerves of *Cmtm5$^{-/-}$* and control mice in dependence of the *Wld^s* mutation at 6 months.

1362 Representative electron micrographs; arrowheads point at pathological profiles. Scale bar,

1363 1µm. **(E)** Quantification of pathological profiles in the optic nerves of 6 months old mice. Note

1364 that *Cmtm5* deletion causes an increased number of pathological profiles, which is reduced by

1365 the presence of the *Wld^s* mutation. Data correspond to optic nerves from 4-5 mice per group

1366 and 20 random non-overlapping EM images analyzed. Unpaired Two-sided Student´s t-test

1367 *Cmtm5$^{wt/wt}$*: p= 0.5107; *Cmtm5$^{-/-}$*: p= 0.0014. Bar graphs give mean ± SEM; data points

1368 represent individual mice.

1369

1370

1371 **Immunoblot Source data files**

1372 **Figure 1A source data 1.** Immunoblot of CMTM5 in Figure 1A

1373 **Figure 1A source data 2.** Immunoblot of PLP in Figure 1A

1374 **Figure 1A source data 3.** Immunoblot of CNP in Figure 1A

1375 **Figure 1A source data 4.** Immunoblot of SIRT2 in Figure 1A

1376

1377 **Figure 1C source data 1.** Immunoblot of CMTM5 in Figure 1C at P15-P24 and 6m-24m

1378 **Figure 1C source data 2.** Immunoblot of PLP in Figure 1C at P15-P24

1379 **Figure 1C source data 3.** Immunoblot of PLP in Figure 1C at 6m-24m

1380 **Figure 1C source data 4.** Immunoblot of CNP in Figure 1C at P15-P24

1381 **Figure 1C source data 5.** Immunoblot of CNP in Figure 1C at 6m-24m

1382 **Figure 1C source data 6.** Immunoblot of SIRT2 in Figure 1C at P15-P24

1383 **Figure 1C source data 7.** Immunoblot of SIRT2 in Figure 1C at 6m-24m

1384

1385 **Figure 1D source data 1.** Immunoblot of CMTM5 in Figure 1D at P15-P24

1386   **Figure 1D source data 2.** Immunoblot of CMTM5 in Figure 1D at 6m-24m

1387   **Figure 1D source data 3.** Immunoblot of PLP in Figure 1D at P15-P24

1388   **Figure 1D source data 4.** Immunoblot of PLP in Figure 1D at 6m-24m

1389   **Figure 1D source data 5.** Immunoblot of CNP in Figure 1D at P15-P24

1390   **Figure 1D source data 6.** Immunoblot of CNP in Figure 1D at 6m-24m

1391   **Figure 1D source data 7.** Immunoblot of SIRT2 in Figure 1D at P15-P24

1392   **Figure 1D source data 8.** Immunoblot of SIRT2 in Figure 1D at 6m-24m

1393

1394   **Figure 2A source data 1.** Immunoblot of CMTM5 and SIRT2 in Figure 2A

1395   **Figure 2A source data 2.** Immunoblot of CNP in Figure 2A

1396   **Figure 2A source data 3.** Immunoblot of PLP in Figure 2A

1397

1398   **Figure 6A source data 1.** Immunoblot of CMTM5 in Figure 6A

1399   **Figure 6A source data 2.** Immunoblot of CNP in Figure 6A

1400   **Figure 6A source data 3.** Immunoblot of SIRT2 in Figure 6A

1401

1402   **Figure 6D source data 1.** Immunoblot of CMTM5 in Figure 6D

1403   **Figure 6D source data 2.** Immunoblot of PLP in Figure 6D

1404   **Figure 6D source data 3.** Immunoblot of SIRT2 in Figure 6D

1405

1406   **Figure 6 Supplement 1A source data 1.** Immunoblot of CMTM5 in Figure 6 Supplement 1A

1407   **Figure 6 Supplement 1A source data 2.** Immunoblot of CAII in Figure 6 Supplement 1A

1408   **Figure 6 Supplement 1A source data 3.** Immunoblot of CNP in Figure 6 Supplement 1A

1409

1410   **Figure 6 Supplement 1B source data 1.** Immunoblot of CMTM5 in Figure 6 Supplement 1B

1411   **Figure 6 Supplement 1B source data 2.** Immunoblot of CAII in Figure 6 Supplement 1B

1412   **Figure 6 Supplement 1B source data 3.** Immunoblot of PLP in Figure 6 Supplement 1B

1413

1414   **Source Data blots labelled.** Immunoblots with the relevant bands labelled.

1415

1416

1417

Feature	*Cmtm5* mutants	*Cnp* mutants	*Plp* mutants
Myelinated axons [%]	Normal	Reduced	Reduced
Myelin thickness	Normal	Trend to thinner myelin	Normal-appearing
Myelin structure	Normal	Inner tongue swellings, myelin outfoldings	Lamella splittings, myelin outfoldings
Axonopathy	Early onset, progressive	Early onset, progressive	Early onset, progressive
Modified by *Wld^S*	Reduction of pathology	No effect	No effect
APP$^+$ axonal swellings	Late onset	Early onset	Early onset
Microgliosis	Late onset	Early onset	Early onset
Astrogliosis	Late onset	Early onset	Early onset
References	This study	Edgar et al., 2009; Lappe-Siefke et al., 2003; Patzig et al., 2016; Rasband et al., 2005	(Edgar et al., 2004; Griffiths I et al., 1998; Klugmann & Schwab, 1997; Patzig et al., 2016)

1418 **Table 1. Comparison of neuropathological features in *Cmtm5, Cnp* and *Plp* mutant mice.**

1419 Neuropathological features in *Cmtm5* cKO, *Cnp$^{-/-}$* and *Plp$^{-/Y}$* mutant mice and key references

1420 are given. APP, amyloid precursor protein.

1421

1422

1423

Antigen	Host species	Method, dilution	Source and Catalog #
α-APP	Mouse	IHC 1:1000	Chemicon (#MAB348)
α-CAII	Rabbit	IB 1:500, IHC 1:300	(Ghandour et al., 1980)
α-CMTM5	Rabbit	IB 1:1000	Proteintech, Pineda (Custom made) Sequence: YRTELMPSTTEGD
α-CMTM5	Rabbit	IHC 1:200	Pineda (Custom made) Sequence: CAFKIYRTELMPSTTEGDQQ
α-CNP	Mouse	IB 1:1000	Sigma Aldrich (#SAB1405637)
α-GFAP	Mouse	IHC 1:200	Novo Castra (#NCL-L-GFAP-GA5)
α-IBA1	Goat	IHC 1:1000	abcam (#ab5076)
α-MAC3	Rat	IHC 1:400	Pharmingen (#553322)
α-PLP	Rabbit	IB 1:2000	A431, (Jung et al., 1996)
α-RBPMS	Guinea Pig	IHC 1:300	Sigma Aldrich (#ABN1376)
α-SIRT2	Rabbit	IB 1:500	abcam (#ab67299)
α-TUJ1	Mouse	IHC 1:1000	Covance (#MMS-435P)
α-mouse HRP	Goat	IB 1:10000	Dianova (# 115-03-003)
α-rabbit HRP	Goat	IB 1:10000	Dianova (# 111-035-003)
α-rabbit Alexa555	Donkey	IHC 1:1000	Dianova (#SBA-3030-32)
α-guinea pig Alexa555	Donkey	IHC 1:1000	Dianova
α-mouse STAR RED	Goat	IHC 1:200	abberior (# STRED- 1001-500UG)
α-rabbit STAR ORANGE	Goat	IHC 1:200	abberior (# STORANGE-1002-500UG)

1424 **Table 2: Antibody information**

1425 IHC, immunohistochemistry; IB, immunoblot

1426
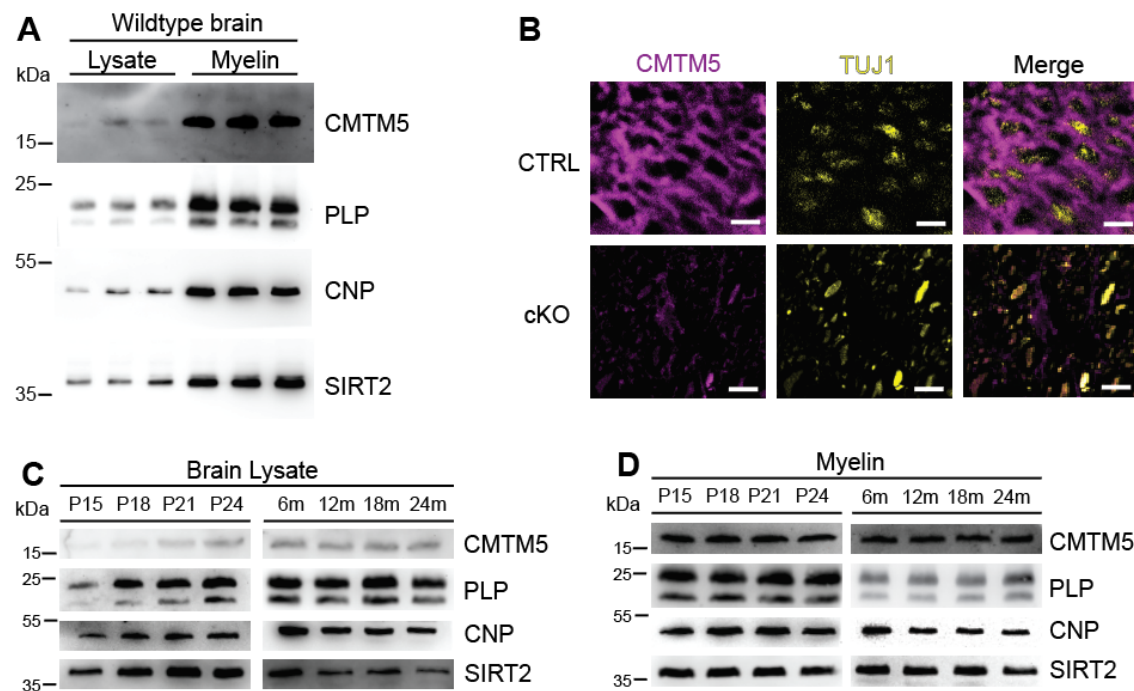
1427

1428
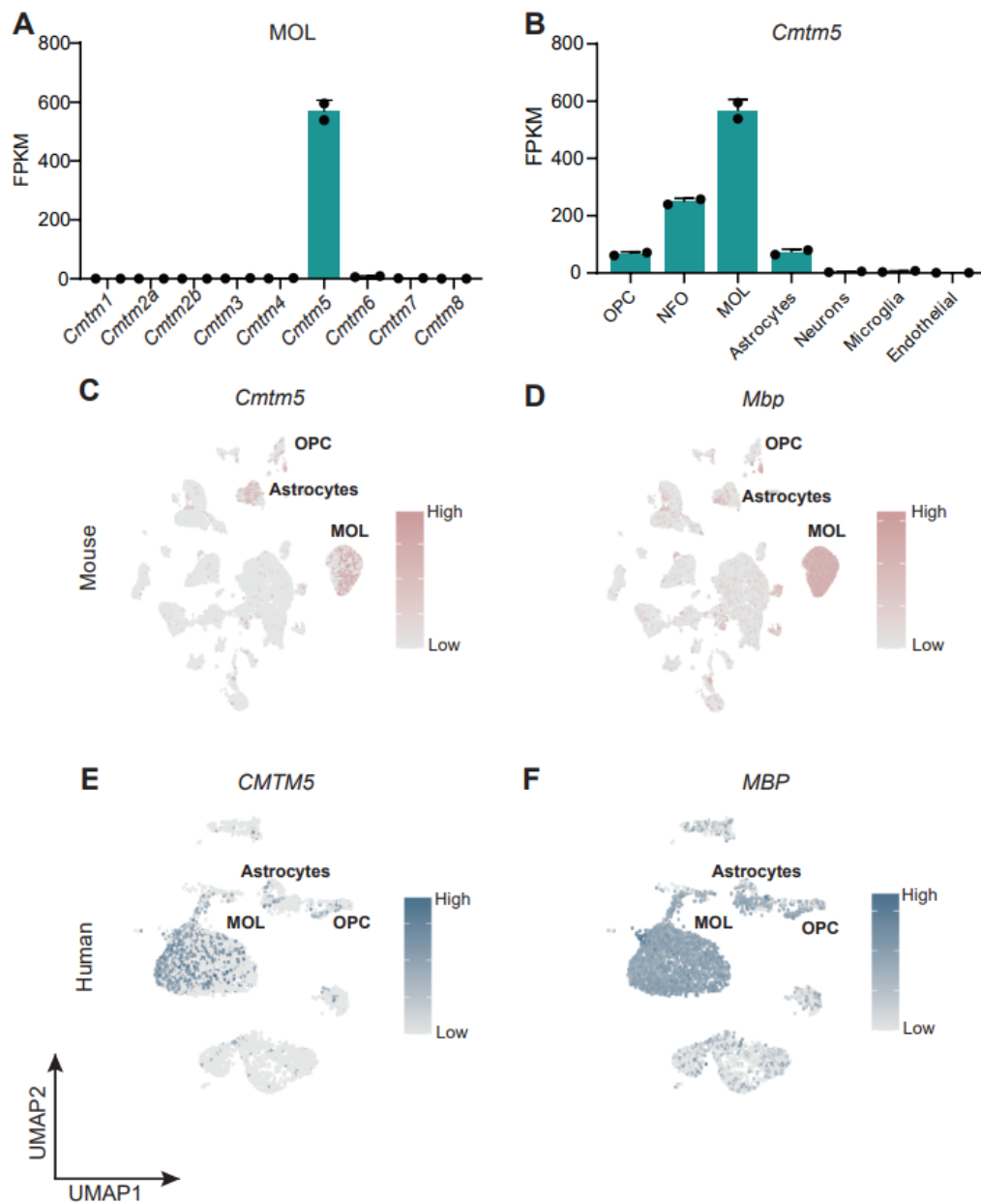
1429

1430

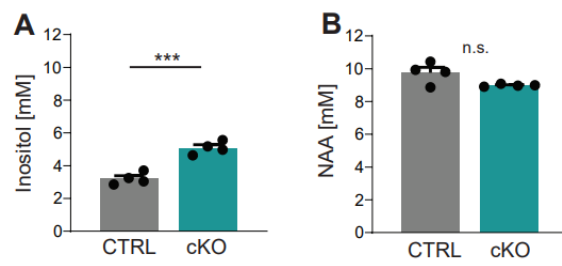Buscham et al., Figure 2
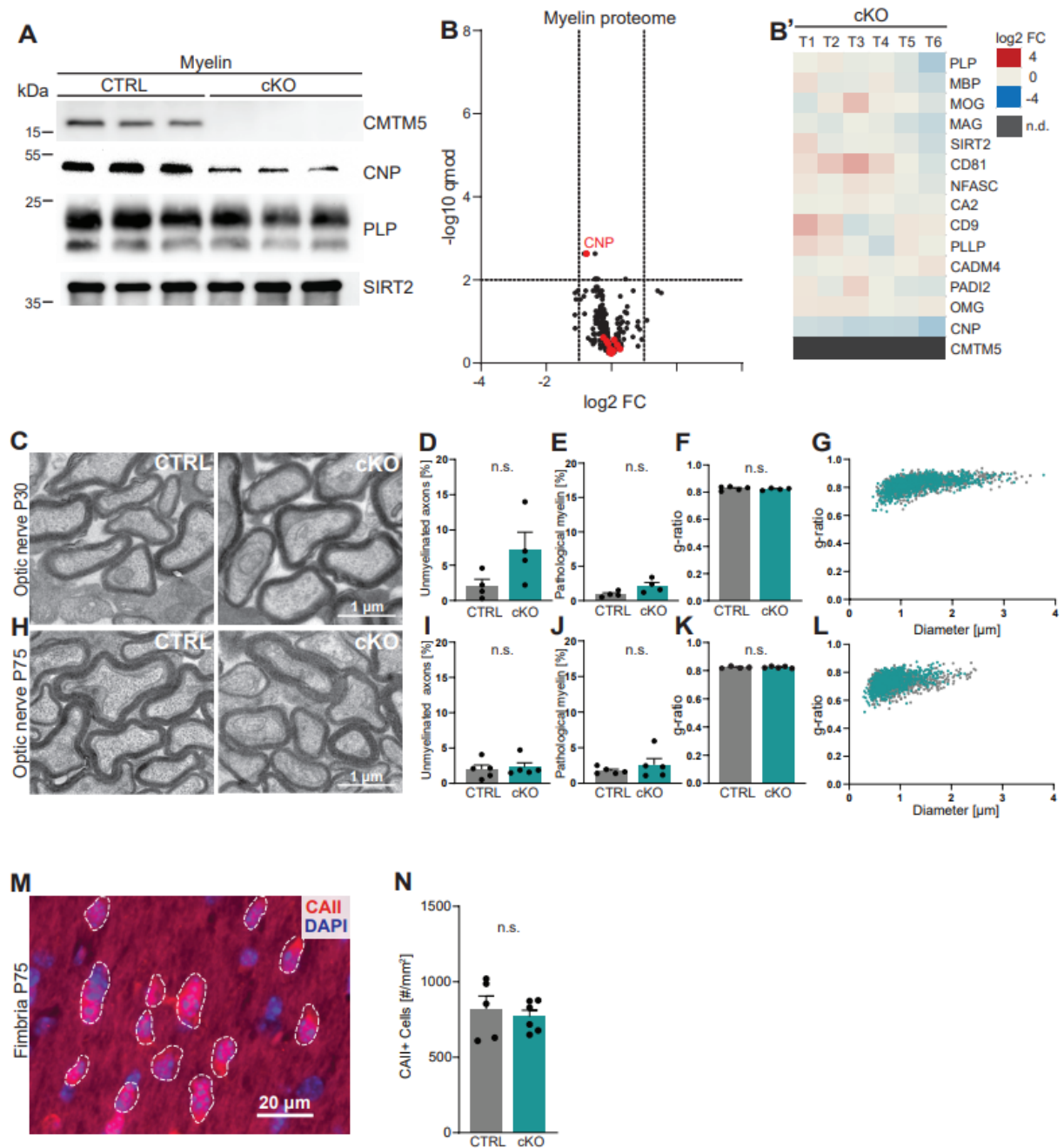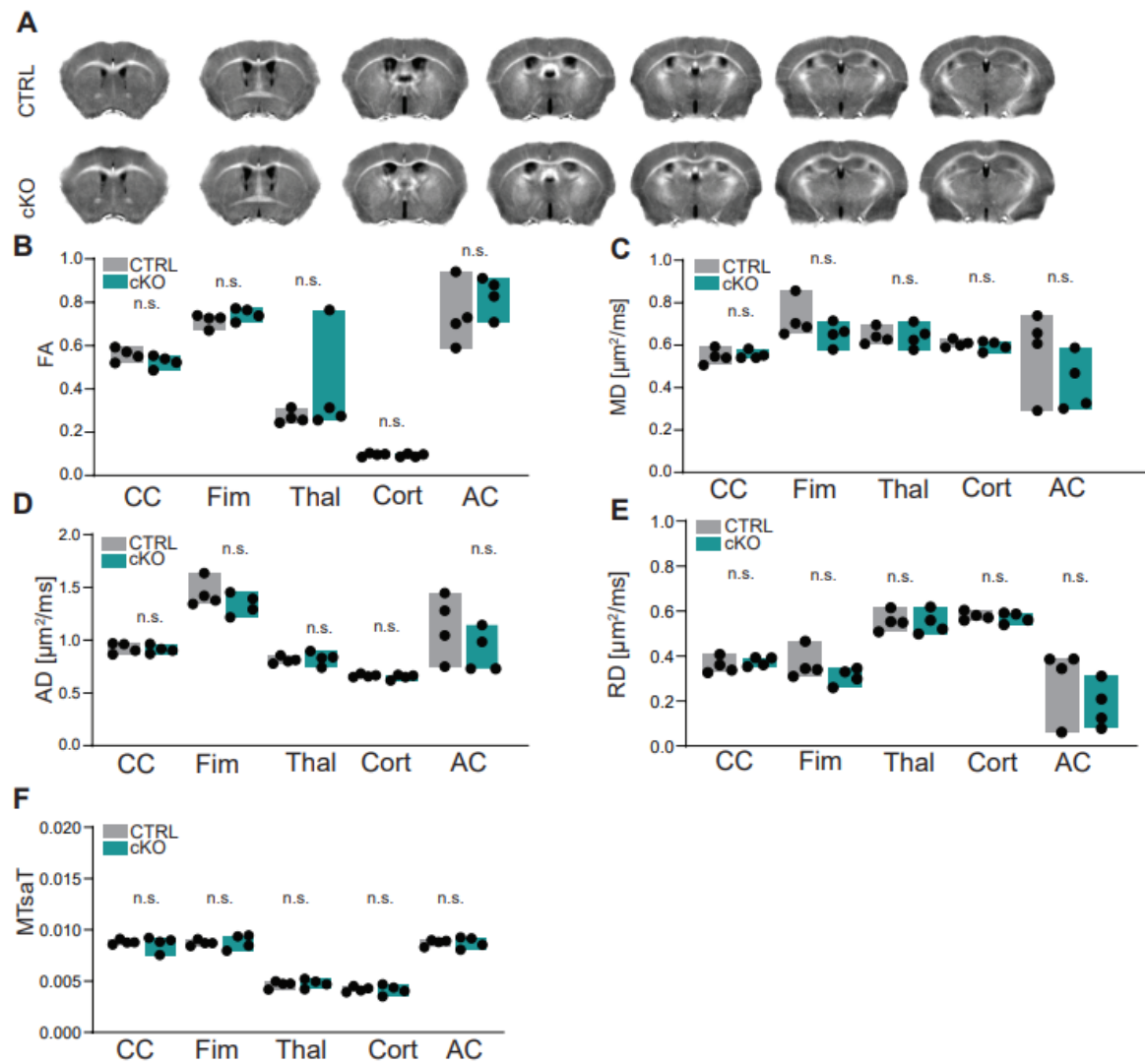
1433

1434

Buscham et al., Figure 3
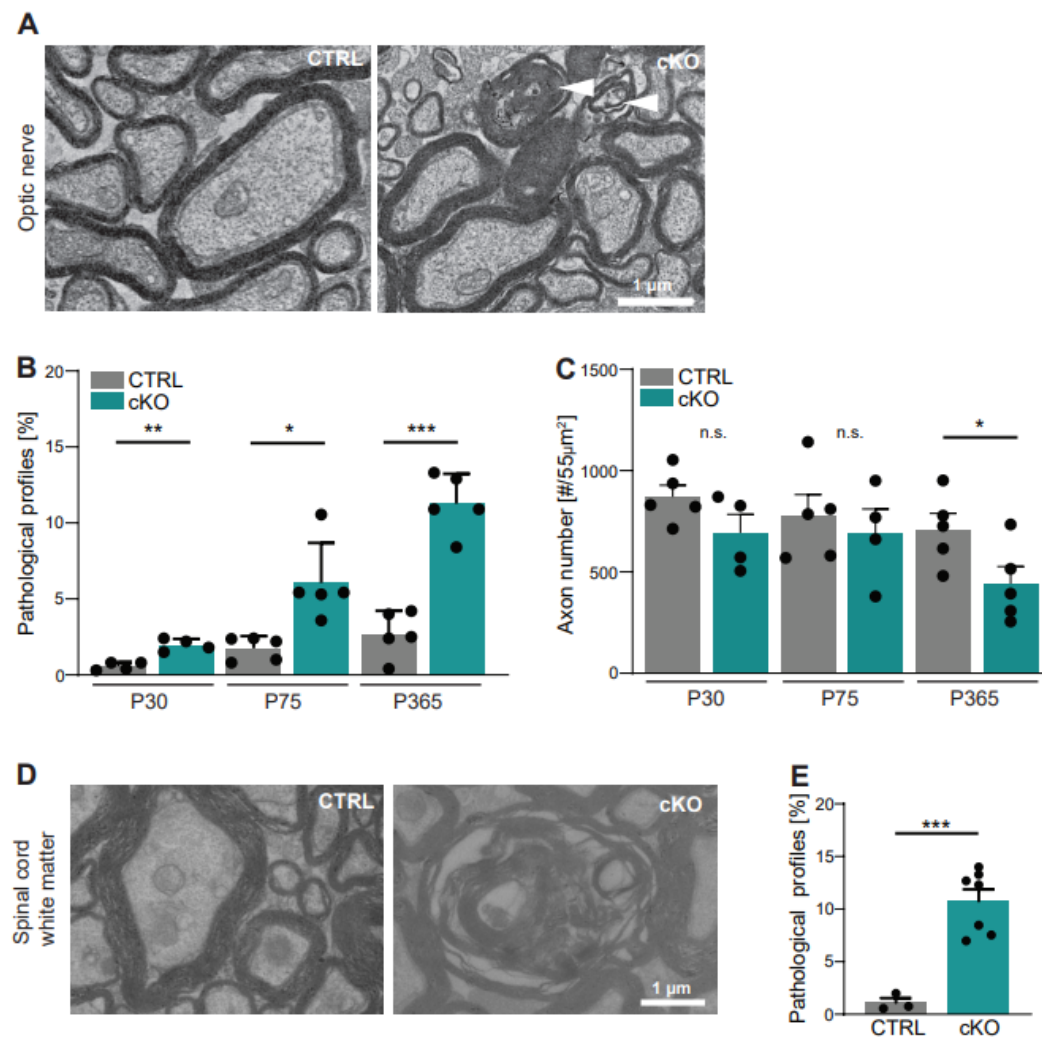
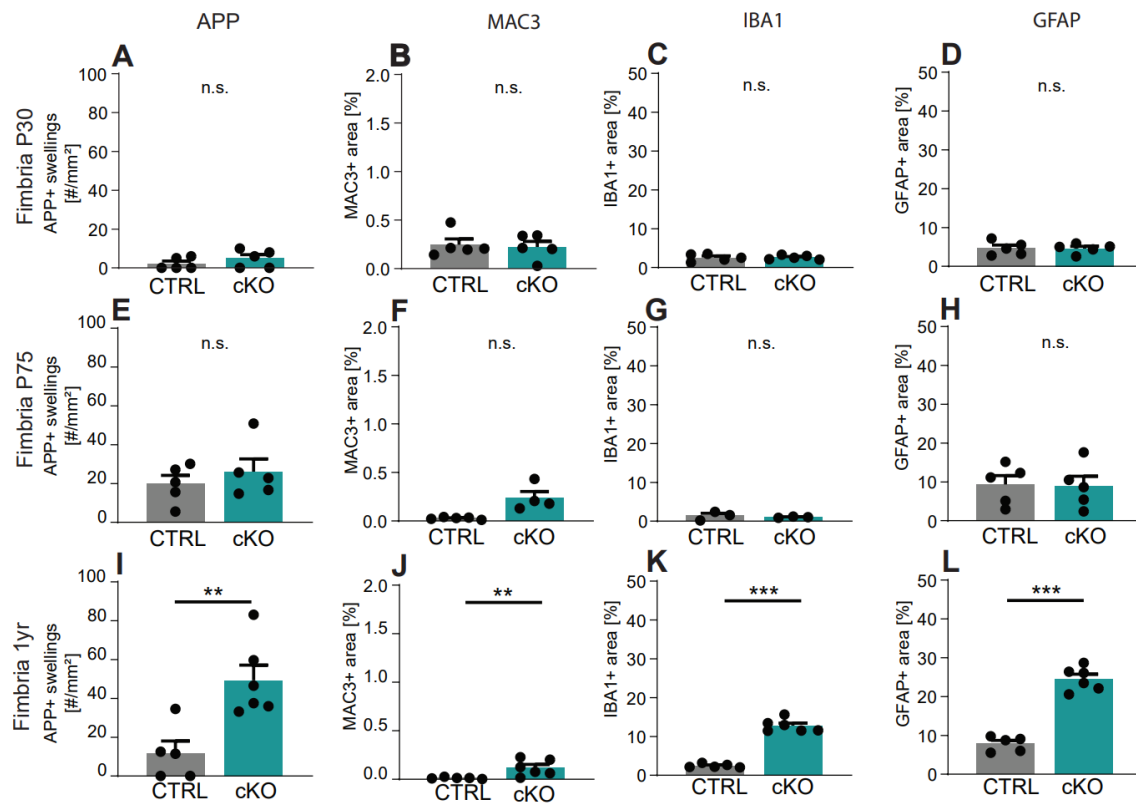

1435

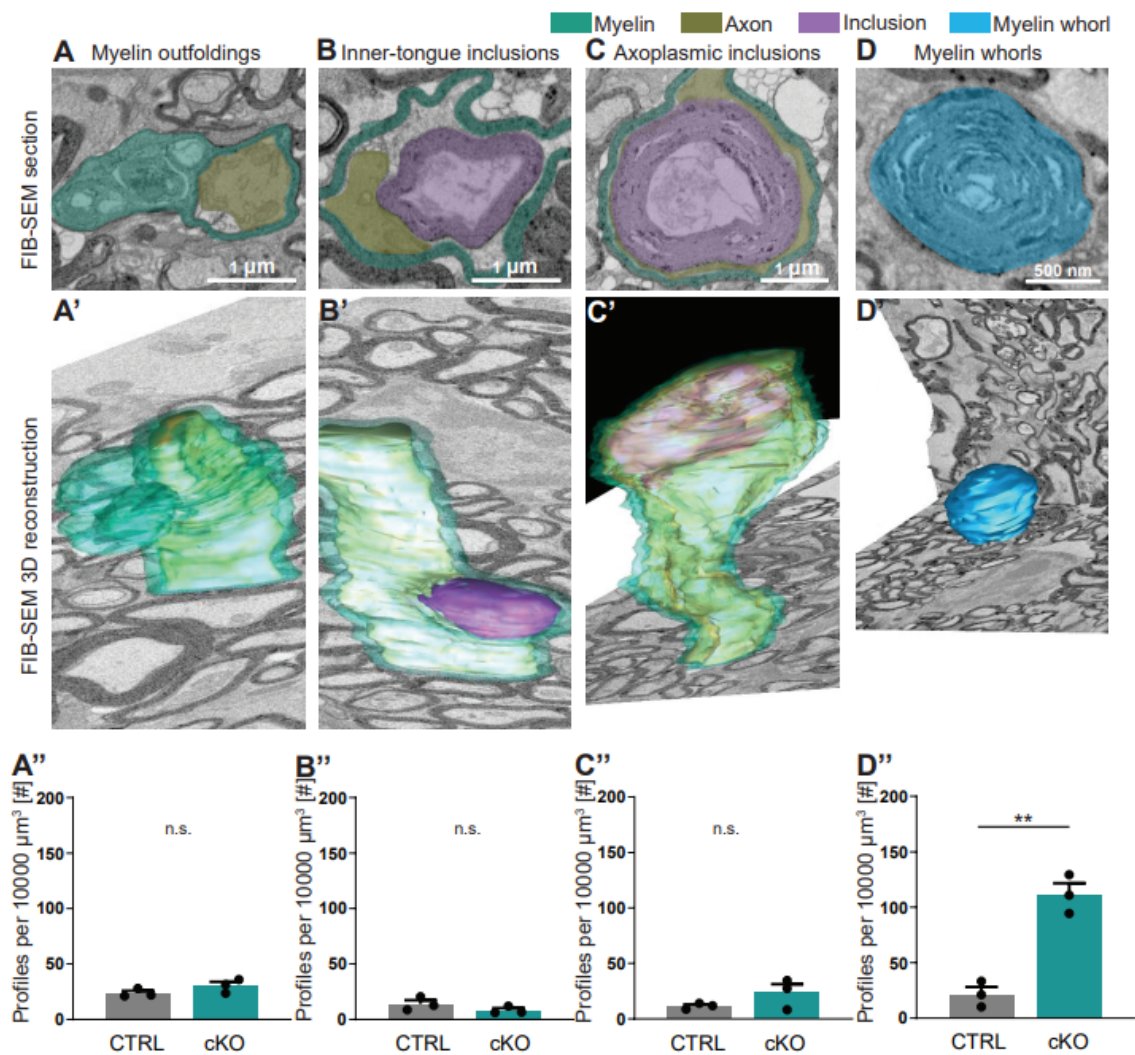1436
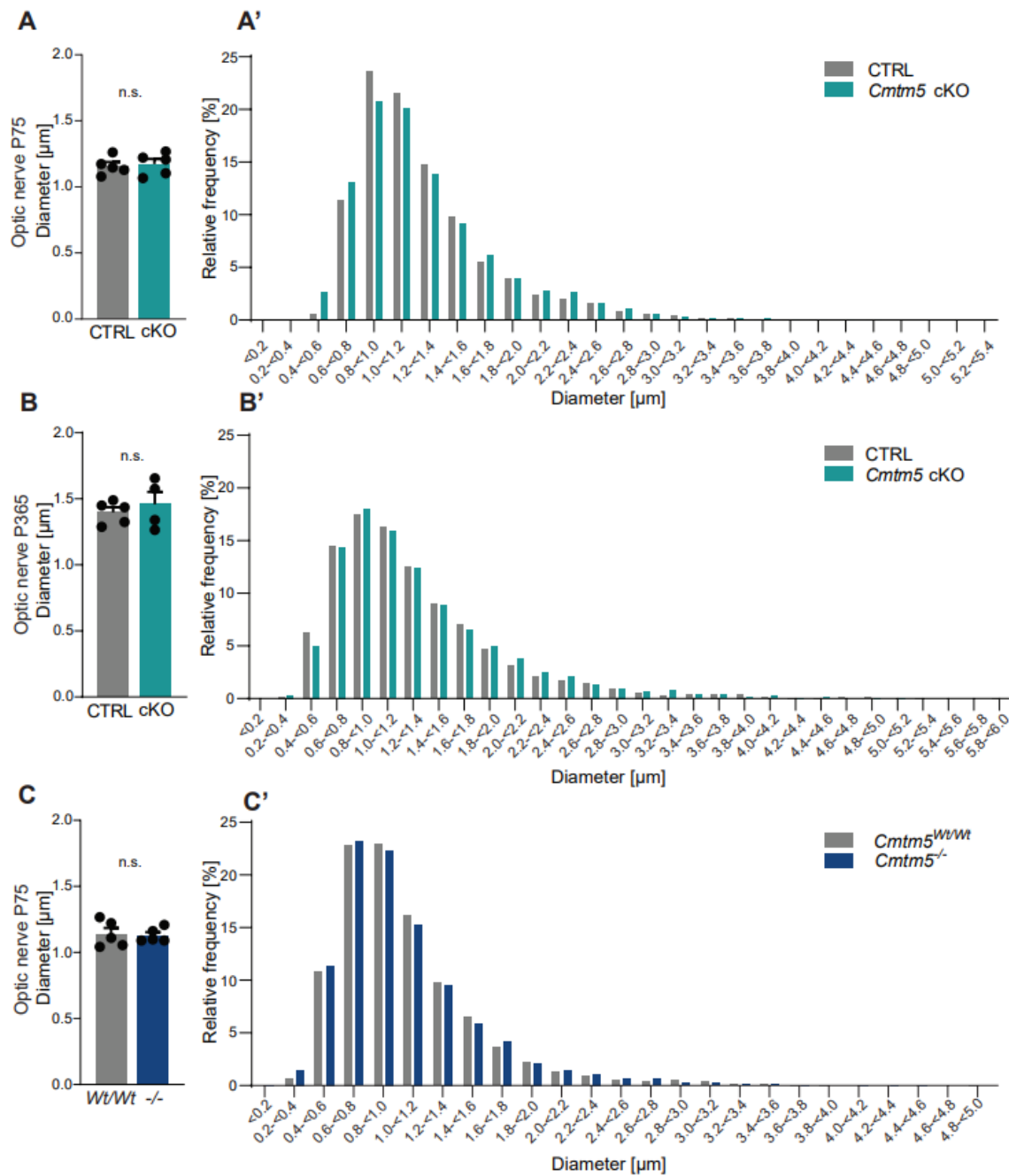
1437

1438

Buscham et al., Figure 3 Supplement 2

1439

1440

Buscham et al., Figure 3 Supplement 3

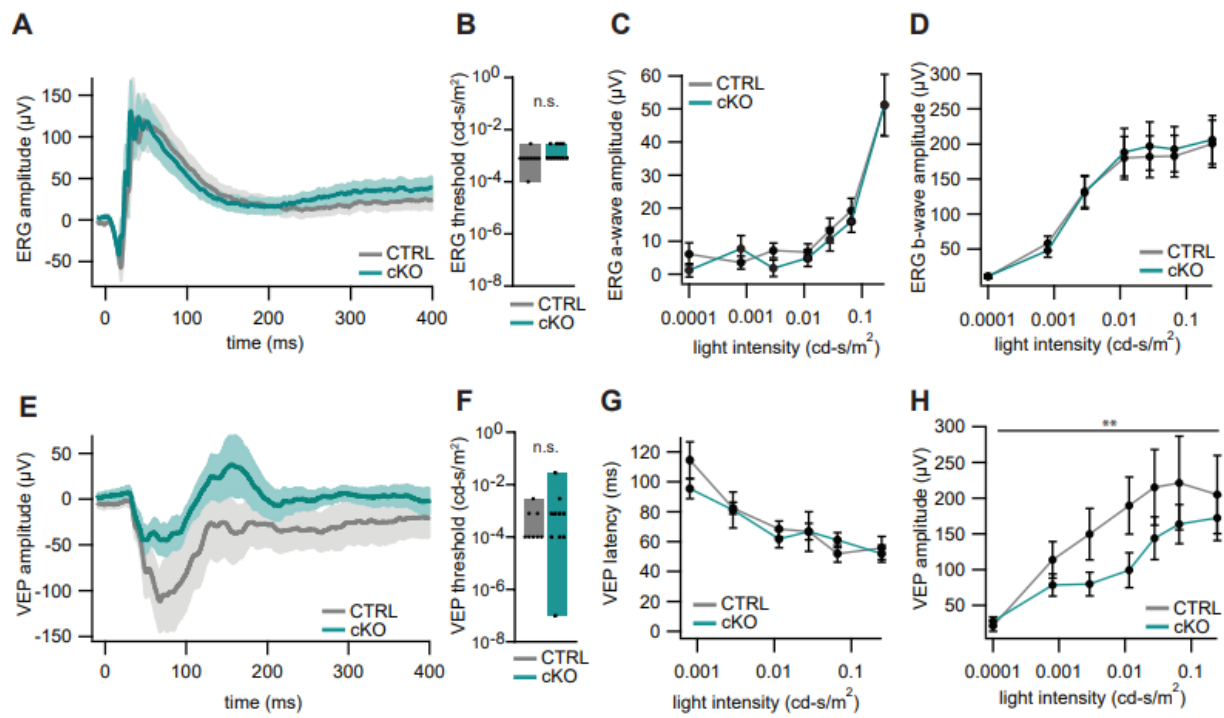

1441

1442

Buscham et al., Figure 4

1443

1444

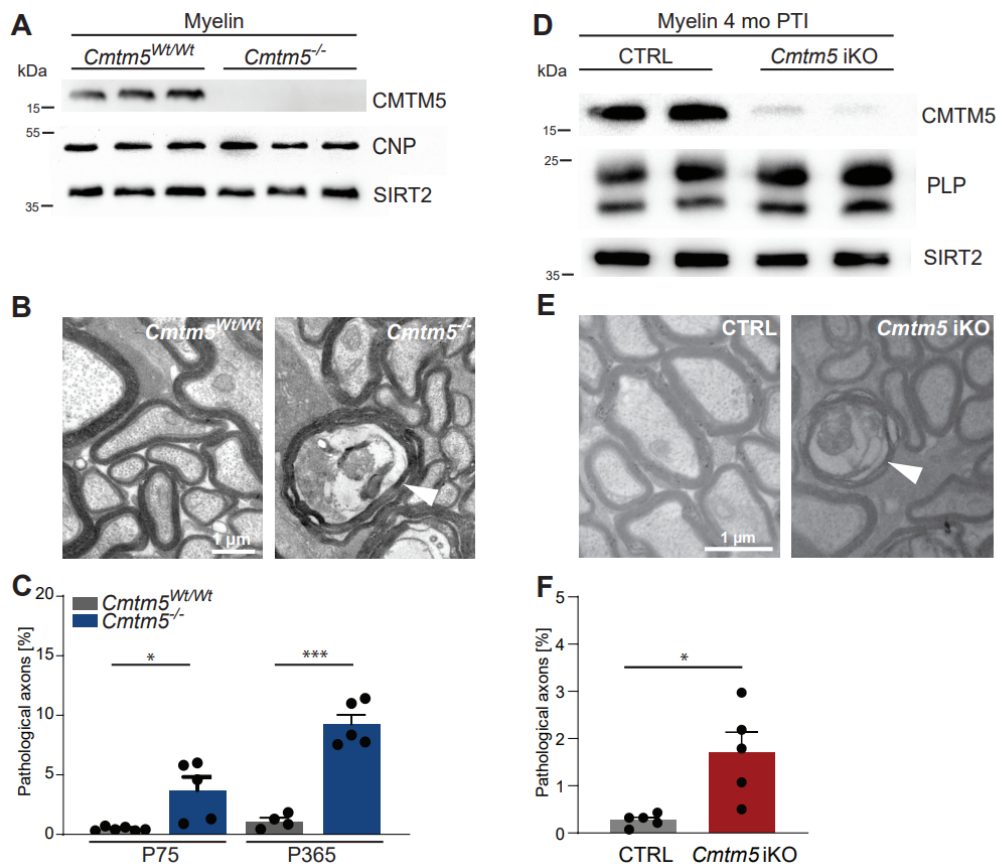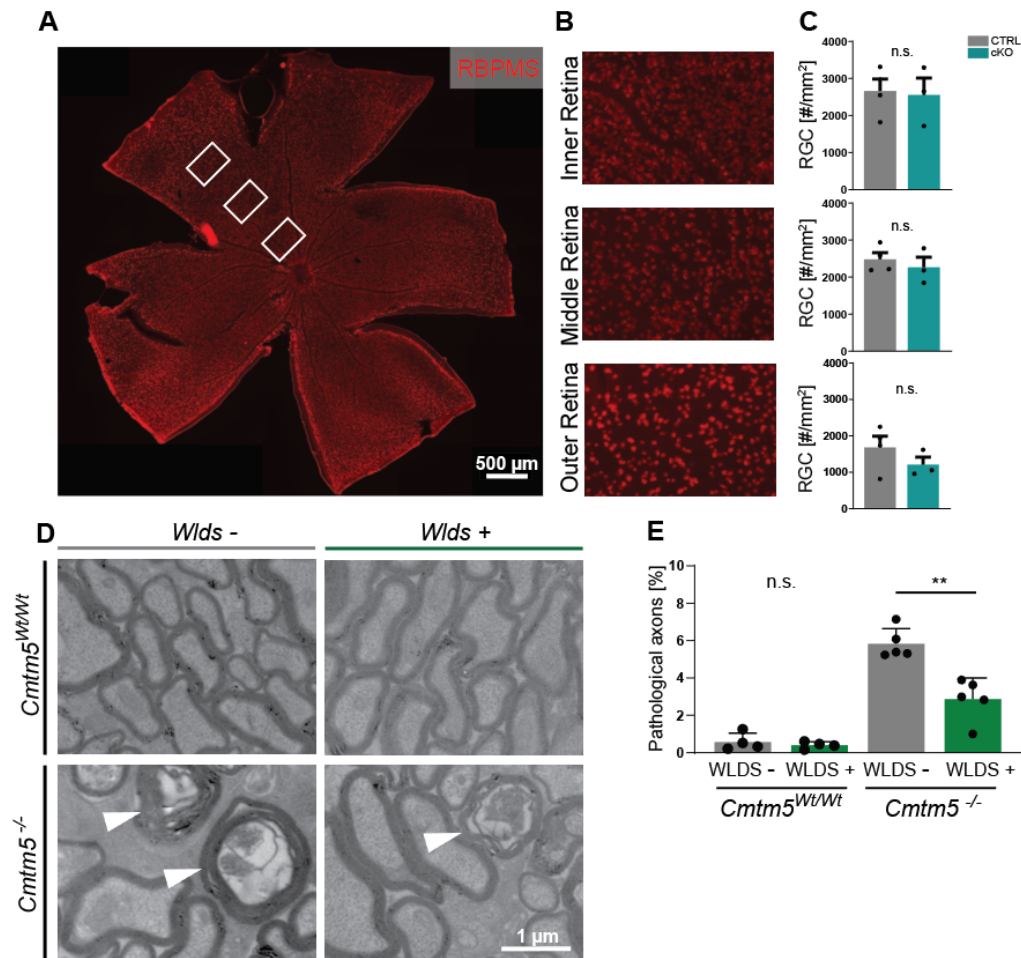1445

1446

1449

1450

1451